

# Kent Academic Repository

## Full text document (pdf)

### Citation for published version

Orlandi, Fabio and Aza, Eleni and Bakaimi, Ioanna and Kiefer, Klaus and Klemke, Bastian and Zorko, Andrej and Aronon, Denis and Stock, Christopher and Tsibidis, George D. and Green, M.A. and Manuel, Pascal and Lappas, Alexandros (2018) Incommensurate atomic and magnetic modulations in the spin-frustrated  $\text{LaMnO}_2$  triangular lattice. *Physical Review Materials*, 2 (7). 074407.

### DOI

<https://doi.org/10.1103/PhysRevMaterials.2.074407>

### Link to record in KAR

<http://kar.kent.ac.uk/67281/>

### Document Version

Author's Accepted Manuscript

#### Copyright & reuse

Content in the Kent Academic Repository is made available for research purposes. Unless otherwise stated all content is protected by copyright and in the absence of an open licence (eg Creative Commons), permissions for further reuse of content should be sought from the publisher, author or other copyright holder.

#### Versions of research

The version in the Kent Academic Repository may differ from the final published version.

Users are advised to check <http://kar.kent.ac.uk> for the status of the paper. **Users should always cite the published version of record.**

#### Enquiries

For any further enquiries regarding the licence status of this document, please contact:

[researchsupport@kent.ac.uk](mailto:researchsupport@kent.ac.uk)

If you believe this document infringes copyright then please contact the KAR admin team with the take-down information provided at <http://kar.kent.ac.uk/contact.html>

## Incommensurate atomic and magnetic modulations in the spin-frustrated $\beta$ -NaMnO<sub>2</sub> triangular lattice

Fabio Orlandi,<sup>1</sup> Eleni Aza,<sup>2,3</sup> Ioanna Bakaimi,<sup>2,\*</sup> Klaus Kiefer,<sup>4</sup> Bastian Klemke,<sup>4</sup> Andrej Zorko,<sup>5</sup> Denis Arčon,<sup>5,6</sup> Christopher Stock,<sup>7</sup> George D. Tsibidis,<sup>2</sup> Mark A. Green,<sup>8</sup> Pascal Manuel,<sup>1</sup> and Alexandros Lappas<sup>2,†</sup>

<sup>1</sup>*ISIS Facility, Rutherford Appleton Laboratory, Harwell Oxford, Didcot OX11 0QX, United Kingdom*

<sup>2</sup>*Institute of Electronic Structure and Laser, Foundation for Research and Technology–Hellas, Vassilika Vouton, 71110 Heraklion, Greece*

<sup>3</sup>*Department of Materials Science and Engineering, University of Ioannina, 451 10 Ioannina, Greece*

<sup>4</sup>*Department Sample Environment and CoreLab Quantum Materials, Helmholtz-Zentrum Berlin für Materialien und Energie GmbH, D-14109 Berlin, Germany*

<sup>5</sup>*Jozef Stefan Institute, Jamova c. 39, 1000 Ljubljana, Slovenia*

<sup>6</sup>*Faculty of Mathematics and Physics, University of Ljubljana, Jadranska c. 19, 1000 Ljubljana, Slovenia*

<sup>7</sup>*School of Physics and Astronomy, University of Edinburgh, Edinburgh EH9 3JZ, United Kingdom*

<sup>8</sup>*School of Physical Sciences, University of Kent Canterbury, Kent CT2 7NH, United Kingdom*



(Received 1 April 2018; published xxxxxx)

The layered  $\beta$ -NaMnO<sub>2</sub>, a promising Na-ion energy-storage material, has been investigated for its triangular lattice capability to promote complex magnetic configurations that may release symmetry restrictions for the coexistence of ferroelectric and magnetic orders. The complexity of the neutron powder diffraction patterns underlines that the routinely adopted commensurate structural models are inadequate. Instead, a single-phase superspace symmetry description is necessary, demonstrating that the material crystallizes in a compositionally modulated  $\mathbf{q} = (0.077(1), 0, 0)$  structure. Here Mn<sup>3+</sup> Jahn-Teller distorted MnO<sub>6</sub> octahedra form corrugated layer stacking sequences of the  $\beta$ -NaMnO<sub>2</sub> type, which are interrupted by flat sheets of the  $\alpha$ -like oxygen topology. Spontaneous long-range collinear antiferromagnetic order, defined by the propagation vector  $\mathbf{k} = (1/2, 1/2, 1/2)$ , appears below  $T_{N1} = 200$  K. Moreover, a second transition into a spatially modulated proper-screw magnetic state ( $\mathbf{k} \pm \mathbf{q}$ ) is established at  $T_{N2} = 95$  K, with an antiferromagnetic order parameter resembling that of a two-dimensional (2D) system. The evolution of <sup>23</sup>Na NMR spin-lattice relaxation identifies a magnetically inhomogeneous state in the intermediate  $T$  region ( $T_{N2} < T < T_{N1}$ ), while its strong suppression below  $T_{N2}$  indicates that a spin gap opens in the excitation spectrum. High-resolution neutron inelastic scattering confirms that the magnetic dynamics are indeed gapped ( $\Delta \sim 5$  meV) in the low-temperature magnetic phase, while simulations on the basis of the single-mode approximation suggest that Mn spins residing on adjacent antiferromagnetic chains, establish sizable 2D correlations. Our analysis points out that novel structural degrees of freedom promote cooperative magnetism and emerging dielectric properties in this nonperovskite type of manganite.

DOI: [10.1103/PhysRevMaterials.00.004400](https://doi.org/10.1103/PhysRevMaterials.00.004400)

### I. INTRODUCTION

Devising cost-efficient chemical routes for multiferroic magnetolectric compounds that foster coupling between spins and other electron degrees of freedom is a fascinating problem of both fundamental and technological interest [1]. Engineering the materials' structure to accommodate unusual coordinations of interacting neighbors offers one such viable but challenging avenue. The perturbation of exchange interactions that emerge from competition due to magnetic frustration [2–4] can select complex spin arrangements that release symmetry restrictions and realize the long-wanted coupling of otherwise mutually exclusive ferroelectric and magnetic orders. In this context, the nonperovskite, two-dimensional (2D) Na-Mn-O oxides are investigated as a testing ground for such a kind of

magnetolectricity. These are rock-salt derivatives of the family  $A^+Me^{3+}O_2$  ( $A =$  alkali metal,  $Me = 3d$  transition metal) delafossites [5,6] that have attracted considerable interest due to their physical and chemical properties. They include, transparent conducting oxides, such as the CuAlO<sub>2</sub> [7], superconductors, like the hydrated variant Na<sub>0.3</sub>CoO<sub>2</sub> · 1.3H<sub>2</sub>O [8] of the P2-Na<sub>y</sub>CoO<sub>2</sub> bronzes [9], multiferroics as AFeO<sub>2</sub> ( $A =$  Na, Ag) [10,11], and cathodic materials for high-capacity Na-ion rechargeable batteries, like P2-Na<sub>y</sub>Mn<sub>1-x</sub>M<sub>x</sub>O<sub>2</sub> ( $x, y \leq 1$ ,  $M =$  Ni, Mg, Li) [12]. Such intercalation materials show high structural flexibility upon alkali metal insertion or extraction and give rise to a rich phase diagram [13]. The crystal chemistry of AMeO<sub>2</sub> allows for polymorphism due to oxygen-layer gliding processes [14]. Consequently, their performance is mediated by phase transitions between nearly degenerate structural types [e.g., designated as O3- ( $3R$ ;  $R-3m$ ) and P2- ( $P6_3/mmc$ )] [12,15], while extended defects (e.g., stacking faults) formed between various crystal domains, render the apparently simple A<sub>x</sub>MeO<sub>2</sub> bronzes metastable. Therefore, new insights on the impact of their inherent compositional

\*Present address: Ioanna Bakaimi, Department of Chemistry, University of Southampton, Southampton SO 171 BJ, UK.

†Corresponding author: lappas@iesl.forth.gr

variation are sought in order to explain their complicated sequences of electronic and structural processes.

Core concepts of materials science point out that when near-degenerate energy states are involved, compositional modulation [16] often emerges as a naturally evolving process that relieves frustration by satisfying the cation-anion chemical requirements, as, for example, in ferroelectrics [17] and shape memory alloys [18,19]. Then, alternatives to traditional crystallographic approaches are necessary in order to understand how subtle structural modulations in correlated transition metal oxides (e.g., cation order and tilting of metal-oxygen coordination polyhedral, etc.) entangle their electron degrees of freedom and lead to novel behavior, extending from heterogeneous catalysis and spin-induced ferroelectricity to high-temperature superconductivity. The ability to control such functional properties, often emerging in the framework of broken symmetries (as in  $\text{TbMnO}_3$  and  $\text{Ni}_3\text{V}_2\text{O}_8$  magnetoelectric materials) [20], relies on understanding the role of residual disorder governing the modulation of atomic positions and magnetic moments. The superspace formalism, previously implemented for the description of modulated chemical crystal structures [21], has grown as a powerful method especially when nuclear and magnetic modulations intertwine in the same phase [22]. Diverse structural types, ranging from perovskites ( $\text{CaMn}_7\text{O}_{12}$  [23],  $\text{Pb}_2\text{MnWO}_6$  [24]) to wolframite-type ( $\text{MnWO}_4$  [25]) modulated structures, which all display symmetry-allowed coupling of electric polarization and magnetization, are illustrative examples of the importance of a robust and efficient treatment of the symmetry of nuclear and magnetic modulations.

The focus here is on two particular polymorphs in the Na-Mn-O system which crystallizes in distorted variants of the  $\text{O}3\text{-NaFeO}_2$  structure ( $3R$  polytype,  $R\text{-}3m$ ) [26]. In these layered compounds the spontaneous deformation of the  $\text{MnO}_6$  octahedra is caused by the Jahn-Teller effect, inherent to the high-spin  $\text{Mn}^{3+}$  cations ( $t_{2g}^3e_g^1$ ;  $S = 2$ ;  $\mu_{\text{eff}} \cong 4.9 \mu_B$ ). Because of this distortion,  $\alpha\text{-NaMnO}_2$  becomes monoclinic ( $C2/m$ ), with flat [27]  $\text{MnO}_6$  sheets [Fig. S1(a) in the Supplemental Material] [28], while  $\beta\text{-NaMnO}_2$  appears to adopt an orthorhombic cell ( $Pmnm$ ), entailing zigzag [29]  $\text{MnO}_6$  sheets [Fig. S1(b)] [28]. The latter polytype is similar to the thermodynamically stable lithiated analog  $\beta\text{-LiMnO}_2$  [30], an important precursor phase for cathode materials in solid-state Li-ion batteries [31]. Moreover, specific challenges facing the Mn-containing systems are governed: (a) by the very similar free-energies of the  $\alpha$ - and  $\beta$ - $\text{NaMnO}_2$  polymorphs [32], which suggest that intermediate phases with compositional modulations could be formed at a very low energy cost, and (b) by the Mn topology (see Fig. S1 in the Supplemental Material) [28] that maps out a triangular lattice [33], inferring some degree of spin frustration that renders these polymorphs sensitive to small perturbations.

In view of the former characteristic, transmission electron microscopy and synchrotron x-ray powder diffraction have shown that on the basis of superspace formalism, planar defects could act as a structure-directing mechanism in the cation-ordered rock-salt-type  $\text{AMeO}_2$  structures, and in particular, the  $\alpha$  and  $\beta$  phases of  $\text{NaMnO}_2$  can be gradually transformed into each other by changing the density of the involved twin planes [33]. Interestingly, the presence of local intergrowths of  $\beta$ -polymorph and stacking faults within the lattice of

the parent  $\alpha\text{-NaMnO}_2$  phase is shown to be controlled in single-crystals grown under optimal conditions [34]. This apparent energy degeneracy between  $\alpha$ - and  $\beta$ -type oxygen coordinations seems to play an important role in determining the particularly high charge capacity ( $\sim 190 \text{ mA h g}^{-1}$ ) of polycrystalline  $\beta\text{-NaMnO}_2$  as an earth-abundant Na-ion cathode [35]. As of the second inherent feature, neutron powder diffraction has shown that despite the considerable spin frustration in  $\alpha\text{-NaMnO}_2$ , Néel order sets in at 45 K [36]. With this concomitant symmetry breaking, a spin gap due to leading quasi-one-dimensional interactions (with a predominant nearest-neighbor exchange interaction of  $J_1 \sim 72 \text{ K}$  [37] and frustrated  $J_2 \cong 0.44 J_1$  [38]; Fig. S1(a) [28]) describes the low-energy magnetic dynamics, while a peculiar magnetostructural inhomogeneity emerges as a consequence of the system's tendency to remove magnetic degeneracy due to spin frustration [39,40]. On the other hand, the magnetic ground state of  $\beta\text{-NaMnO}_2$  is less well understood from the experimental point of view. Theoretical calculations, though, predict that a spin model with two-dimensional couplings [ $J_1 \sim 70 \text{ K}$  nearest neighbor and  $J_3 \sim 57 \text{ K}$  next nearest neighbor; Fig. S1(b)] [28] and a weaker frustrated interaction ( $J_2 \sim 13 \text{ K}$ ) are likely to describe the experimental magnetic susceptibility. This material also manifests an abundant quasiperiodic arrangement of defects [33]. Moreover, room-temperature  $^{23}\text{Na}$  solid-state nuclear magnetic resonance (NMR) spectra supported by first-principles DFT computations identified a wealth of local structural rearrangements, entailing a trade-off between the majority  $\beta$ -type nanodomains and those of the  $\alpha$ -like phase upon electrochemical cycling of sodium [41].

The present contribution provides a powerful neutron powder diffraction insight on  $\beta\text{-NaMnO}_2$ , highlighting that this challenging material is stabilized by near equivalent in energy lattice conformations. The strength of superspace formalism has been utilized to describe the structure on the basis of a single-phase model, entailing an incommensurate compositional modulation. The latter is depicted as a coherent intergrowth of two types of  $\text{NaMnO}_2$  layers, reflecting the  $\alpha$ - and  $\beta$ -type oxygen coordinations, and is shown to determine the material's physical properties. We illustrate the implications of the modified lattice topology, with its intrinsic extended defects, on the successive magnetic phase transitions. Furthermore, temperature-dependent  $^{23}\text{Na}$  NMR and inelastic neutron scattering experiments point out that the magnetic dynamics are gapped, while the influence of the magnetic order on the electric dipole order is also reflected in the temperature- and field-dependent magnetocapacitance studies.

## II. EXPERIMENTAL METHODS

Polycrystalline  $\beta\text{-NaMnO}_2$  samples were synthesized by a high-temperature solid-state chemistry protocol reported before [33], while phase identification was undertaken by x-ray powder diffraction (XRPD) experiments carried out on a Rigaku D/MAX-2000H rotating Cu anode diffractometer.  $\beta\text{-NaMnO}_2$  specimens were air sensitive and all post-synthesis handling was carried with the aid of an Ar-circulating MBRAUN anaerobic glove box.

DC magnetic susceptibility as a function of temperature ( $5 \leq T \leq 300 \text{ K}$ ) was measured on 20 mg batches of powder

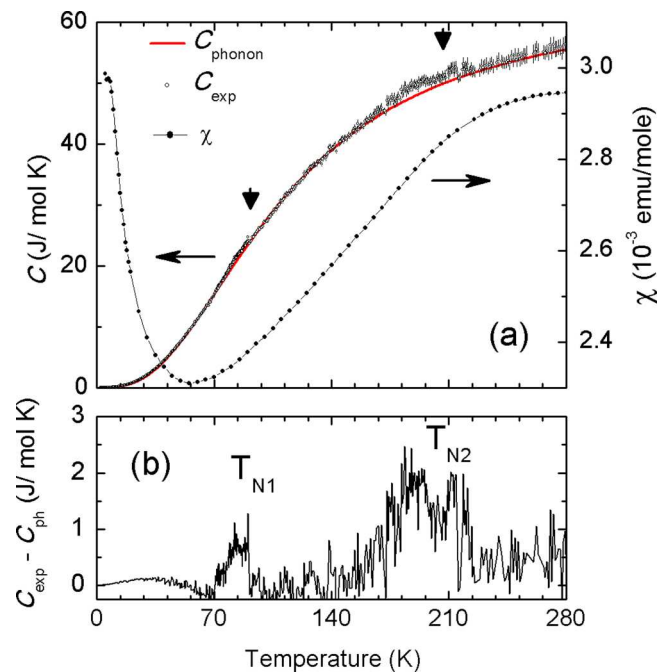
187 samples with a superconducting quantum interference device  
 188 (SQUID) magnetometer (Quantum Design, MPMS-XL7) under  
 189 a moderate magnetic field ( $H = 20$  mT). Heat capacity ( $C$ )  
 190 was measured at zero field on a cold-pressed pelletized powder  
 191 sample by means of the relaxation technique, utilizing a physical  
 192 property measurement system (Quantum Design, PPMS).

193 NMR measurements on the  $^{23}\text{Na}$  nucleus (nuclear spin  
 194  $I = 3/2$ ) were performed on a powder sample sealed in  
 195 a pyrex sample holder.  $^{23}\text{Na}$  NMR spectra and spin-lattice  
 196 relaxation rate  $1/T_1$  were recorded between 50 and 300 K  
 197 in a magnetic field of 8.9 T using a solid-echo and inversion  
 198 recovery pulse sequences, respectively. Wide-line  $^{23}\text{Na}$  NMR  
 199 powder data were obtained as sums of individual spectra  
 200 acquired by changing the measurement frequency in 50 kHz  
 201 steps over  $\pm 3$  MHz around the  $^{23}\text{Na}$  reference frequency,  
 202  $\nu_0 = 100.5234$  MHz, which was determined from a 0.1 M  
 203 NaCl solution. The spin-lattice relaxation rate measurements  
 204 were performed at the position of the central line.

205 Neutron powder diffraction data were collected on the  
 206 WISH diffractometer [42], operating at the second target station  
 207 (TS2) at the ISIS pulsed neutron source in the UK. WISH,  
 208 with its high brilliance, is particularly optimized for providing  
 209 high resolution at long  $d$  spacing required for magnetic studies.  
 210 For this purpose, a 2.7 g polycrystalline sample was loaded  
 211 in a 8 mm V-can, which was then sealed with indium wire  
 212 inside a high-quality, He-circulating anaerobic glove box. An  
 213 Oxford Instrument liquid helium cryostat was used for the  
 214 temperature dependent diffraction experiments. Data analysis  
 215 was performed by using the Jana2006 software [43] for the  
 216 Rietveld refinements, whereas the group theory analysis was  
 217 performed with the help of the ISODISTORT software [44].

218 Inelastic neutron scattering work was performed on the  
 219 MARI direct geometry chopper spectrometer (ISIS, UK) and  
 220 also on the DCS spectrometer (NIST, USA). Experiments on  
 221 MARI used incident energies  $E_i = 85$  and 150 meV, with  
 222 a Gd Fermi chopper spun at 300 and 450 Hz, respectively.  
 223 Measurements on DCS were done with an incident energy of  
 224  $E_i = 14.2$  meV. A 7.3 g of a powder sample was loaded in an  
 225 annular aluminum sachet that was placed inside a cylindrical  
 226 Al-can for the ISIS experiment, while a 5 g sample was loaded  
 227 in V-can for the NIST experiment. In either case the cans  
 228 were sealed with indium wire and they were cooled at low  
 229 temperatures with a top-loaded closed-cycle refrigerator. All  
 230 data has been corrected for background and also phonons from  
 231 the structural lattice. For the MARI data, the background plus  
 232 phonon contribution to the scattering at each energy transfer  
 233 was estimated from the high angle detector banks where  
 234 magnetic scattering is suppressed owing to the  $\text{Mn}^{3+}$  form  
 235 factor. We have fit the high angle and high momentum detectors  
 236 at a fixed energy transfer to the form  $L(Q) = L_0 + L_1 Q^2$ , with  
 237  $L_0$  capturing the background and  $L_1$  providing an estimate  
 238 of the phonon scattering.  $L(Q)$  was then used to estimate  
 239 the background and phonon scattering at low momentum  
 240 transfers and then it was subtracted. For data taken on DCS,  
 241 the background was estimated by using the requirement for  
 242 detailed balance as discussed previously [45].

243 The dielectric permittivity of  $\sim 3$  mm pellets of pressed  
 244 polycrystalline samples, without electrodes attached on the  
 245 two flat surfaces, was studied at the CoreLab for Quantum  
 246 Materials in the Helmholtz-Zentrum, Berlin, with a 14 T



247 FIG. 1. Temperature dependent (a) zero-field cooled dc magnetic  
 248 susceptibility  $\chi(T)$  (right axis) under an applied field of 20 mT, and  
 249 the heat capacity  $C(T)$  (left axis) of  $\beta$ - $\text{NaMnO}_2$ . The red line over the  
 250  $C(T)$  data is the calculated phonon contribution to the specific heat  
 251  $C_{\text{ph}}(T)$  (see text). (b) The heat capacity remaining after subtracting  
 252 the  $C_{\text{ph}}(T)$  contribution from the experimental  $C(T)$  depicts two  
 253 anomalies assigned as  $T_{N1}$  and  $T_{N2}$ .  
 254  
 255  
 256

247 PPMS system. The home-made setup is tailored for dielectric  
 248 constant measurements in a capacitorlike arrangement. It gives  
 249 the possibility to select between an AH 2700A ultraprecision  
 250 capacitance bridge, for relatively low frequencies (50 Hz–  
 251 20 kHz) or a Solatron 1260 impedance/gain phase analyzer,  
 252 for the high-frequency region up to 32 MHz; the latter is  
 253 being used together with a 1296A dielectric interface system  
 254 in order to cope with ultralow capacitance levels. A Lakeshore  
 255 370 temperature controller was utilized to cover a broad  
 256 temperature range ( $5 \leq T \leq 180$  K).

### 257 III. RESULTS AND DISCUSSION

#### 258 A. Macroscopic properties

259 The temperature dependent magnetic susceptibility  $\chi(T)$   
 260 of the different  $\text{NaMnO}_2$  polymorphs qualitatively appears  
 261 similar, with exception of the presence of a broad maximum  
 262 ( $\sim 200$  K for  $\alpha$ -polytype) [36], which apparently shifts to  
 263 higher temperature in the  $\beta$  phase [Fig. 1(a)]. Such a broad  
 264 feature is a general characteristic of low-dimensional antiferro-  
 265 magnetic systems. However, from  $\chi(T)$  data alone no evidence  
 266 for a transition to a long-range ordered state is observed.

267 On the other hand, the heat capacity  $C(T)$  measured in  
 268 zero magnetic field displays several very weak anomalies  
 269 (Fig. 1), possibly of magnetic origin. In order to highlight  
 270 these features, we first estimated the phonon contribution to the  
 271 specific heat  $C_{\text{ph}}(T)$  and subtracted it from the experimentally  
 272 measured heat capacity. Here  $C_{\text{ph}}(T)$  assumes a sum of Debye  
 273 contributions ( $2 < T < 280$  K), following the procedure used

274 before for other low-dimensional spin systems [46,47]:

$$C_{\text{ph}}(T) = 9R \sum_{i=1}^2 C_i \left( \frac{T}{\theta_D^{(i)}} \right)^3 \int_0^{x_D^{(i)}} \frac{x^4 e^x}{(e^x - 1)^2} dx, \quad (1)$$

275 with  $R$  ( $8.314 \text{ J mol}^{-1} \text{ K}^{-1}$ ) the gas constant,  $\theta_D^{(i)}$  is the Debye  
 276 temperature, and  $x_D^{(i)} = \theta_D^{(i)}/T$ , while fitting was based on  
 277 an optimization approach using the minimum number of  
 278 free parameters. In our case, the  $C_{\text{ph}}(T)$  was approximated  
 279 by two Debye functions, addressing the relatively different  
 280 atomic masses of the constituent element-coupled vibrations  
 281 (cf. Na-O and Mn-O) in the  $\beta$ -NaMnO<sub>2</sub>. This yielded the fitting  
 282 parameters  $C_1 = 0.55(2)$ ,  $C_2 = 2.0(2)$  and  $\theta_D^{(1)} = 287(22) \text{ K}$ ,  
 283  $\theta_D^{(2)} = 510(15) \text{ K}$  [Fig. 1(a)]. The vanishingly small magnitude  
 284 of  $C(T)$  at very low temperatures, in accord with the  $\beta$ -  
 285 phase insulating nature, agrees well with the  $\propto T^3$  term that  
 286 corresponds to phonons [Eq. (1)].

287 The outcome of the subtraction of  $C_{\text{ph}}(T)$  from the total heat  
 288 capacity is shown in Fig. 1(b). As the corresponding anomalies  
 289 in the differential  $C(T)$  are very small, pointing to some  
 290 sensitivity to the defects in the lattice structure (*vide infra*),  
 291 and the estimated phonon part uncertainties are high, they  
 292 render further analysis to assess the differential  $C(T)$  as a likely  
 293 magnetic contribution  $\Delta S_{\text{mag}} = \int \frac{C_{\text{mag}}(T)}{T} dT$ , unfavorable at  
 294 this stage. The identification, though, of the two fairly broad  
 295 humps centered at  $\sim 95$  ( $T_{N2}$ ) and  $\sim 200 \text{ K}$  ( $T_{N1}$ ), would suggest  
 296 that  $\beta$ -NaMnO<sub>2</sub> undergoes two transitions. These qualitative  
 297  $C(T)$  characteristics therefore require further study to inquire  
 298 about the role of magnetic interactions in such phase changes.

### 299 B. <sup>23</sup>Na NMR dynamics near the transitions

300 A critical aspect of many macroscopic thermodynamic  
 301 properties is the role of the material's microscopic dynamical  
 302 response. Techniques capable of detecting spin dynamics on  
 303 a local scale, such as solid-state <sup>23</sup>Na NMR, can therefore be  
 304 helpful to understand the complex behavior of  $\beta$ -NaMnO<sub>2</sub>.  
 305 The <sup>23</sup>Na NMR powder spectra of  $\beta$ -NaMnO<sub>2</sub> were measured  
 306 between room temperature and 50 K, where they become very  
 307 broad and, consequently, the signal becomes very weak and  
 308 difficult to measure [Fig. 2(a)]. At 300 K, the spectrum has  
 309 a characteristic powder line shape for a quadrupole  $I = 3/2$   
 310 nuclei with the quadrupole asymmetry parameter of  $\eta \approx 0$ . A  
 311 closer inspection of the satellite ( $\pm 3/2 \leftrightarrow \pm 1/2$ ) transitions  
 312 of the 300 K spectrum terminated around  $\pm \nu_Q = \pm 1.28 \text{ MHz}$   
 313 from the narrow central transition ( $1/2 \leftrightarrow -1/2$ ) line [upper  
 314 inset to Fig. 2(a)] shows that the expected singularity is  
 315 rounded, which is consistent with a high degree of Na local  
 316 site disorder. Here  $\nu_Q$  is the <sup>23</sup>Na quadrupole frequency. On  
 317 cooling below  $T_{N1}$ , there is almost no change of the central  
 318 transition line. However, a close inspection of the <sup>23</sup>Na NMR  
 319 satellite line reveals that a shoulder starts to gradually broaden  
 320 well beyond  $\pm \nu_Q$ . This is clearly seen as a growth of the  
 321 NMR signal intensity on both sides of the satellite shoulder  
 322 [lower inset of Fig. 2(a)]. As the positions of the satellite  
 323 shoulder remain nearly at the same frequency, the quadrupole  
 324 frequency must also remain the same through the transition  
 325 at  $T_{N1}$ . This suggests that no structural deformation takes  
 326 place in the vicinity of the Na site, corroborating that the high

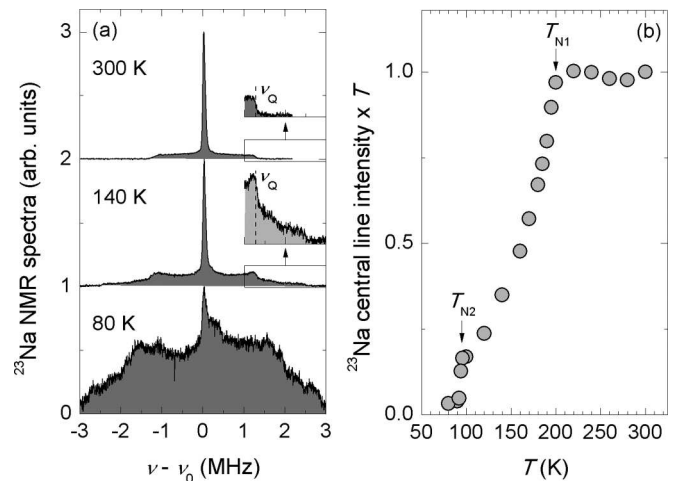


FIG. 2. (a) Normalized <sup>23</sup>Na NMR powder spectra of  $\beta$ -NaMnO<sub>2</sub> revealing two different magnetic regimes that evolve with temperature lowering. The spectra are shifted vertically for clarity. The insets point to a specific part of the spectra, where the quadrupolar frequency is indicated by the vertical dashed line. (b) The temperature dependence of the <sup>23</sup>Na NMR central line intensity multiplied by temperature for  $\beta$ -NaMnO<sub>2</sub>. The arrows indicate the two transition temperatures  $T_{N1}$  and  $T_{N2}$ .

327 temperature transition ( $T_{N1}$ ) is magnetic in origin. Moreover,  
 328 below  $T_{N1}$  the intensity of the sharp central peak multiplied  
 329 by temperature (to counterbalance the changing Boltzmann  
 330 population) starts to progressively decrease with decreasing  
 331 temperature below  $T_{N1}$  [Fig. 2(b)]. The broadening of the NMR  
 332 line beyond the satellites can thus be attributed to growing  
 333 internal magnetic fields at certain Mn ion sites, while the  
 334 gradual wipeout of the central line below  $T_{N1}$  [Fig. 2(b)] reveals  
 335 that the high-temperature paramagnetic-like signal vanishes  
 336 only gradually, as it remains present at all temperatures below  
 337  $T_{N1}$ . This leads us to the important conclusion that the magnetic  
 338 state below  $T_{N1}$  is inhomogeneous. On further cooling below  
 339  $T_{N2}$ , the <sup>23</sup>Na NMR line shape broadening becomes really  
 340 pronounced as the spectrum becomes completely dominated  
 341 by the broad distribution of internal (hyperfine) magnetic  
 342 fields and the sharp central peak almost disappears. These line  
 343 shape changes verify that  $\beta$ -NaMnO<sub>2</sub> indeed undergoes two  
 344 successive transitions to magnetically ordered states, at  $\sim 200$   
 345 and  $\sim 95 \text{ K}$ , in agreement with the assignment of subtle peaks  
 346 in the differential  $C(T)$  as magnetic transitions [Fig. 1(b)].

347 Additional information about the two magnetic transitions  
 348 is deduced from the <sup>23</sup>Na spin-lattice relaxation rate  $1/T_1$ ,  
 349 which was determined from fitting of <sup>23</sup>Na magnetization  
 350 recovery curves [Fig. 3(a)] to the magnetic-relaxation model  
 351 for  $I = 3/2$  [48],

$$M(t) = M_0 \left[ 1 - s \left( 1/10 e^{-\left(\frac{t}{T_1}\right)^\alpha} + 9/10 e^{-\left(\frac{t}{T_1}\right)^\alpha} \right) \right]. \quad (2)$$

352 Here  $s < 1$  accounts for imperfect inversion of <sup>23</sup>Na nuclear  
 353 magnetization after the initial  $\pi$  pulse, while  $\alpha$  stands for  
 354 a stretching exponent. In the high-temperature paramagnetic  
 355 (PM) regime,  $1/T_1$  is nearly temperature independent,  $1/T_1 =$   
 356  $35(1) \text{ s}^{-1}$  [Fig. 3(b)]. Such temperature independence is in  
 357 fact anticipated for an exchange-coupled antiferromagnetic  
 358

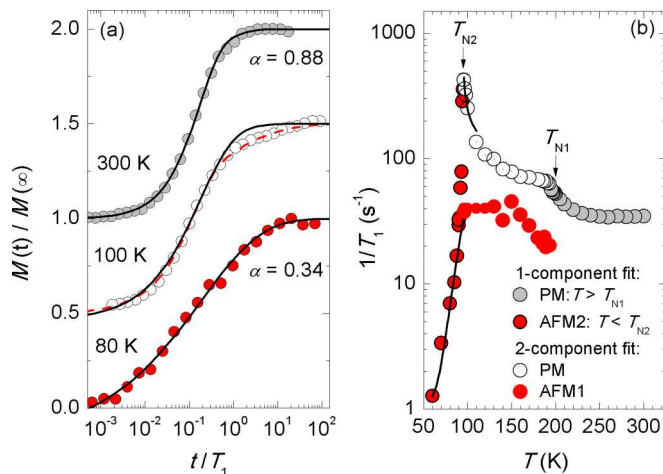


FIG. 3. (a) Normalized magnetization-recovery curves at a few selected temperatures. The data sets are shifted vertically for clarity. The solid lines are fits of a stretched single-component magnetic-relaxation model for  $I = 3/2$  [Eq. (2), see text], while the dashed line corresponds to the fit with two such components. Please note that significantly different stretching exponent  $\alpha$  is found for temperatures above  $T_{N1}$  and below  $T_{N2}$ . (b) The temperature dependence of the spin-lattice relaxation rate for  $\beta$ -NaMnO<sub>2</sub>. The arrows indicate the two transition temperatures. A double-component fit is needed in the intermediate temperature regime  $T_{N2} < T < T_{N1}$ . The solid lines indicate a critical type of behavior for  $T > T_{N2}$  and an activated one for  $T < T_{N2}$  (see text for details).

(AFM) insulator in the paramagnetic phase. The stretching exponent is  $\alpha = 0.88$  [Fig. 3(a)]; a value slightly below 1 implying a small distribution of relaxation rates expected in experiments on powder samples. The transition to the magnetic state at  $T_{N1}$  is accompanied by a sizable steplike increase in the  $1/T_1$  value to  $1/T_1 = 66(5) \text{ s}^{-1}$  and a gradual reduction of the stretching exponent [Fig. 3(a)]. The latter indicates that the distribution of the spin-lattice relaxation times suddenly starts increasing below  $T_{N1}$  thus indicating growing magnetic inhomogeneity between  $T_{N1}$  and  $T_{N2}$  which is in accord with the line shape changes [Fig. 2(a)]. In fact, as two-step magnetization-recovery curves are clearly observed below  $T_{N1}$  [e.g., measurement taken at 100 K shown in Fig. 3(a)], the fit of the magnetization recovery curves in the  $T_1$  experiment is significantly improved if two relaxation components are included. Here the relative intensity of one of the components (AFM1) increases at the expense of the second PM component, the latter in close analogy to the wipeout effect of the narrow central line [Fig. 2(b)].

We stress that no obvious critical fluctuations leading to diverging  $1/T_1$  could be detected at  $T_{N1}$ . The likely reason is the nature of magnetic fluctuations, which according to the expression  $\frac{1}{T_1} = \frac{2\gamma_n^2 k_B T}{(\gamma_n \hbar)^2} \sum_{q\rho} A_q^\rho A_{-q}^\rho \frac{\chi''(q^\rho, \omega)}{\omega}$  (where  $A_q$  denotes the hyperfine coupling of the  $^{23}\text{Na}$  nuclei with the electronic magnetic moments,  $\chi''$  is the imaginary part of the dynamical susceptibility, and  $\omega$  is the Larmor frequency), could be filtered out in the  $1/T_1$  measurements for highly symmetric Na (octahedral) sites. On the other hand, on approaching the lower transition temperature at  $T_{N2}$ , the  $1/T_1$  of the paramagnetic PM component is rapidly enhanced, suggesting the onset of critical

fluctuations. A phenomenological fit of the critical model  $1/T_1 = A + B(T - T_{N2})^{-p}$  to the PM data in the temperature range between  $T_{N2}$  and 110 K, yields the critical exponent  $p = 0.45(10)$  for  $A = 66(5) \text{ s}^{-1}$  and  $T_{N2} = 95.0(5) \text{ K}$  [Fig. 3(b)]. Such critical enhancement demonstrates that the magnetic fluctuations that govern the transition at  $T_{N2}$  cannot be filtered out anymore at the Na site. This is also consistent with the observed dramatic  $^{23}\text{Na}$  NMR line shape changes [Fig. 2(a)]. The temperature dependence of the other component (AFM1), which we attribute to the already magnetically ordered regions in the sample, is much more subtle [Fig. 3(b)]. Finally, at  $T < T_{N2}$ , the two components in the magnetization recovery curves are not obvious anymore [Fig. 3(a)], so we resort back to a single-exponential fit [Eq. (2)]. However, a very low stretching exponent of 0.34 has to be employed. Such a strikingly low value of  $\alpha$  indicates an extremely broad distribution of relaxation times, hence a broad distribution of local magnetic environments below  $T_{N2}$ . At the same time  $1/T_1$  is strongly suppressed below  $T_{N2}$  and exhibits an activated type of dependence [ $1/T_1 \propto T^2 \exp(-\Delta/T)$ , Fig. 3(b)], indicating the opening of an excitation gap  $\Delta$  in the low-temperature phase.

### C. Crystallographic structure

Critical to understanding such transformations is the way magnetic ions are arranged in the underlying lattice structure that establishes nearest-neighbor exchange terms and stabilizes nondegenerate ground states. High quality data collected on the WISH diffractometer enables the analysis of the crystallographic structure of  $\beta$ -NaMnO<sub>2</sub>. The main reflections of the neutron powder diffraction (NPD) pattern are consistent with the  $Pm\bar{m}n$  space group, with cell parameters  $a_o = 4.7851(2) \text{ \AA}$ ,  $b_o = 2.8570(8) \text{ \AA}$ ,  $c_o = 6.3287(4) \text{ \AA}$ , at 300 K. The Rietveld refinement of the main nuclear reflections (300 K), with the  $Pm\bar{m}n$  model [29] [Mn1 in 2b position  $z = 0.617(5)$ , Na1 in 2b  $z = 0.125(4)$ , O1 in 2a  $z = 0.365(6)$ , and O2 in 2a  $z = 0.872(6)$ ], suggests a significant degree of “antisite” defects between the Mn and Na sites that leads to an average occupation of  $\sim 80:20$  (see Fig. S2, Supplemental Material) [28]. Moreover, the refinement points to an unexpectedly large value for the oxygen thermal parameter [ $U_{\text{iso}} \sim 0.038(2) \text{ \AA}^2$ ]. The use of anisotropic temperature factors in the refinement results in a clear elongation of the thermal ellipsoids along the  $c$  direction (see Fig. S2) [27] indicating strong positional disorder. Following this suggestion we split the two oxygen positions along the  $c$  axis and the refinement converged to a splitting of  $\sim 0.5 \text{ \AA}$  and  $\sim 70:30$  occupancy of the resultant sites, with normal isotropic thermal parameters [ $U_{\text{iso}} \sim 0.015(2) \text{ \AA}^2$ ]. It is worth stressing that the split and especially the occupancy of O1 and O2 resemble the antisite occupancy of the Mn and Na atoms; in particular, as shown in Fig. S2 this distortion is needed to satisfy the coordination requirements of the Na and Mn cations.

A crucial feature of the 300 K NPD pattern, in association with the above analysis, is the presence of additional reflections that could be ascribed to a nuclear modulation (Fig. 4). In support of this comes earlier transmission electron microscopy (TEM) work on  $\beta$ -NaMnO<sub>2</sub> [33], where it was pointed out that formation of planar defects establishes short-ranged ordered

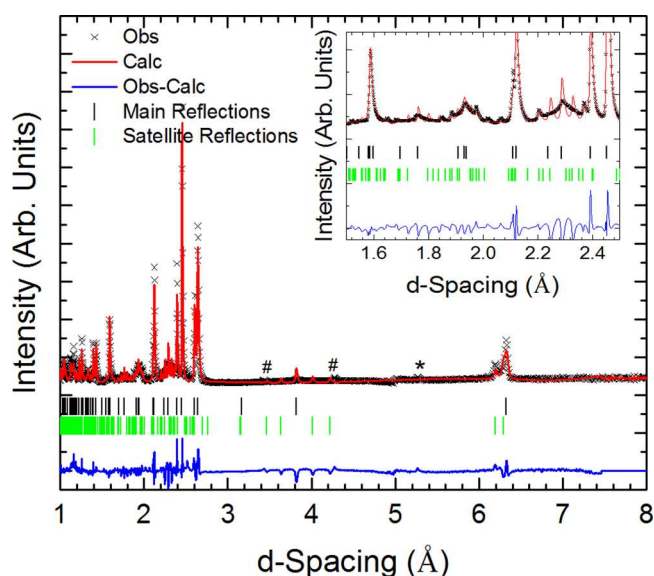


FIG. 4. Rietveld plot at 300 K for the  $\beta$ - $\text{NaMnO}_2$  structure in the  $Pm\bar{m}n(\alpha 00)000$  superspace group. Inset: Zoom of the low  $d$ -spacing region inferring that stacking faults and defects give rise to a peculiarly broadened profile function. In both panels observed (black crosses), calculated (red line), and difference (blue line) patterns are shown. The tick marks indicate the calculated position of the main (black ticks) and satellite reflections (green ticks). The asterisk marks the main reflection from the  $\alpha$ - $\text{NaMnO}_2$  impurity, whereas the hashtags indicate, for example, two satellite peaks that are slightly off with respect to the calculated Bragg position indicating the possibility of the other two components of the modulation vector to be different from zero (see text for details).

regions that locally (i.e., on the length scale of a few unit cells) follow the stacking sequence of  $\text{NaMnO}_2$  layers characteristic of either the  $\alpha$  or the  $\beta$  phases. Importantly, long-period stacking sequences, with a modulation vector  $\mathbf{q} = (\alpha 00)\alpha \approx 0.1$  (consistent with the cell choice reported in the present work), were also required for indexing the additional satellite peaks observed in both electron and synchrotron x-ray diffraction data. From a LeBail fit of the WISH data we obtained an optimal modulation vector  $\mathbf{q} = (0.077(1), 0, 0)$ , accounting for satellites up to the second order in the NPD pattern. Some small satellite reflections, however, are sliding off the calculated position (Fig. 4), suggesting that the other two components of the modulation vector may be slightly different from zero. Refinements where the other two components of  $\mathbf{q}$  were allowed to vary proved unstable and did not lead to reasonable results. The obtained value of  $\mathbf{q}$  is near the commensurate  $1/13$  position, which explains why the  $1/6$  value used before in the synchrotron x-ray diffraction patterns indexed well a large number of satellite peaks.

The observation of the satellite reflections in both NPD and TEM measurements and the refinement of the average nuclear structure indicate the possibility of a compositional modulation in the structure that can be modeled through the superspace formalism [49,50]. The theory of  $(3 + D)$  superspace groups, introduced by de Wolff (1974, 1977) [51,52], is widely used to describe the symmetry of commensurate and incommensurate modulated structures. In order to understand the NPD pattern

of WISH we therefore used a  $(3+1)$ -dimensional superspace approach considering an occupational modulation for all the sites in the average nuclear structure. In order to derive the possible superspace groups we performed group symmetry analysis with the help of the ISODISTORT Software Suite [44] starting from the refined average structure and the propagation vector  $\mathbf{q} = (\alpha 00)$ . Having taken into account the observed reflection conditions and the symmetry properties of the modulation vector, the symmetry analysis led to the  $Pm\bar{m}n(\alpha 00)000$  superspace group as the best solution, corresponding to the  $\Sigma_1$  irreducible representations (IRs), with order parameter direction (OPD)  $P(\sigma, 0)$  [53].

To account for the compositional modulation a steplike (Crenel) function is introduced for every site in the structure. The Crenel function is defined as [54]

$$p(x_4) = 1 \in \langle x_4^0 - \Delta/2, x_4^0 + \Delta/2 \rangle,$$

$$p(x_4) = 0 \notin \langle x_4^0 - \Delta/2, x_4^0 + \Delta/2 \rangle, \quad (3)$$

where  $x_4$  is the internal (fourth) coordinate in the  $(3+1)D$  approach and  $\Delta$  is the width of the occupational domain centered at  $x_4^0$  ( $\Delta$  corresponds also to the average fractional occupancy of the site). The modulation functions on the same cation site are constrained to be complementary, meaning that in every point of the crystal the site is occupied (this results in the equations  $\Delta[\text{Mn}_i] + \Delta[\text{Na}_i] = 1$  and  $x_4[\text{Mn}_i] = 1 - x_4[\text{Na}_i]$  for each cation site). For the split oxygen positions we introduce a similar constraint, imposing that in any position in the crystal we have the superposition of the two split sites. Regarding the origin along the fourth axis, the superspace group constrains this value to two equivalent values: 0 and 0.5, thus making the choice trivial. Moreover, an additional constraint is introduced regarding the two Mn/Na sites. The electron diffraction measurements, reported by Abakumov *et al.* [33], suggest that the quasiperiodic stacking sequences of the  $\text{NaMnO}_2$  layers entail coherent stacking faults, a feature which points out that their modeling can be reduced to the alternation sequence of the Na and Mn cations. We followed a similar approach for the modeling of the NPD pattern assuming that the steplike functions were constrained to have in every  $\text{NaMnO}_2$  plane the right Mn/Na ordering, that is to say, when one site switches from Mn to Na the other changes from Na to Mn. The crystallographic model built in this way was employed for qualitative Rietveld refinements. Broad, asymmetric reflections throughout the NPD pattern, mainly due to defects (e.g., stacking faults) and strain, make such analysis hard to optimize, raising the agreement factors and making a quantitative refinement difficult. The Rietveld plot, over a wide  $d$ -spacing range, is shown in Fig. 4 and the associated reliability factors are  $R_p = 8.81\%$ ,  $R_{wp} = 12.73\%$ ,  $R_{\text{main}} = 9.96\%$ ,  $R_{\text{sat}} \pm 1 = 15.41\%$ ,  $R_{\text{sat}} \pm 2 = 14.79\%$ . Despite the apparent reflection broadening, our model shows good agreement for the modulated parts of the profile, especially obvious in the relatively short  $d$ -spacing region of the pattern (inset in Fig. 4). The crystallographic parameters of the compositionally modulated  $\beta$ - $\text{NaMnO}_2$  at 300 K, on the basis of a  $(3+1)D$  Rietveld analysis with the  $Pm\bar{m}n(\alpha 00)000$  superspace group [ $a = 4.7852(4) \text{ \AA}$ ,  $b = 2.85701(8) \text{ \AA}$ ,  $c = 6.3288(4) \text{ \AA}$ ,  $\alpha = 0.077(1)$ ], are compiled in Table S1 [28].

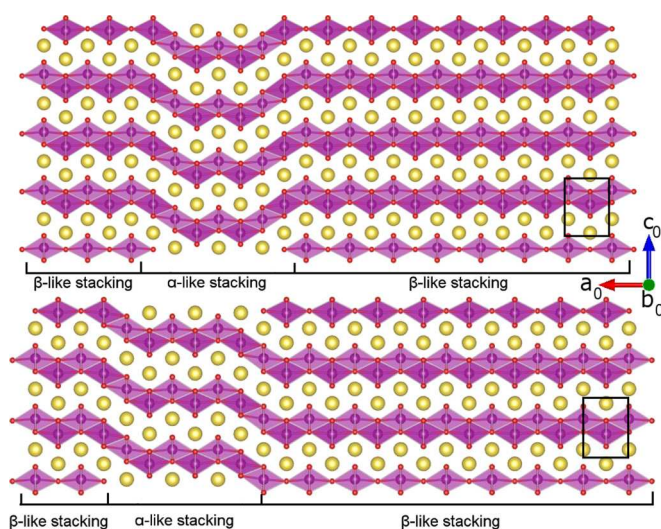


FIG. 5. Projection of the structure in the  $ac$  plane, depicting the refined incommensurate compositional modulated structure; two types of stacking changing between the  $\text{NaMnO}_2$  polymorphs are shown. The violet atoms represent the Mn, the yellow ones the Na, and the red spheres the oxygen atoms. The small rectangle indicates the unit cell of the average  $Pmmn$  structure (see Fig. S1).

528 This single-phase structural model, despite the presence  
 529 of low intensity reflections ascribable to a small amount of  
 530 the  $\alpha$  phase and  $\text{MnO}$  (Fig. 4), takes into account almost  
 531 all the satellites present in the NPD pattern of the  $\beta$  phase,  
 532 as compared to the two-phase description on the basis of  
 533 the  $B2/m(\alpha\beta 0)00$  superspace group derived before from the  
 534 analysis of the synchrotron x-ray powder diffraction data [33].  
 535 The nuclear structure model obtained here is shown in Fig. 5.  
 536 This is consistent with the one proposed by Abakumov *et al.*  
 537 [33], entailing coherent intergrowth of stacking sequences of  
 538  $\text{NaMnO}_2$  layers along the  $\mathbf{a}_0$  axis, characteristic of the  $\alpha$ - and  
 539  $\beta$ -polytypes. It may be considered as good approximation to  
 540 the real chemical phase, as planar defects, seen by electron  
 541 microscopy, could violate the idealized Crenel-type function  
 542 used in the present analysis of the NPD data. In this model, the  
 543  $\text{MnO}_6$  octahedra throughout the structure display strong Jahn-  
 544 Teller distortion (see Fig. S3 [28], for oxygen-cation distances  
 545 in the (3+1)D approach), with four short bonds below  $2 \text{ \AA}$   
 546 and two long ones around  $2.4 \text{ \AA}$ , in a fashion analogous to the  
 547  $\alpha$ - $\text{NaMnO}_2$  [36]. On the other hand, while Na is also octahe-  
 548 drally coordinated to oxygen, the distances involved are longer  
 549 due to its larger ionic radius. Moreover, in an effort to visualize  
 550 the degree of compositional modulation in the  $\beta$ - $\text{NaMnO}_2$   
 551 structure, Fourier maps of the observed structure factor (Fig. 6)  
 552 involving the atomic sites in the  $zx_4$  plane were computed on  
 553 the basis of the observed NPD intensities and the calculated  
 554 phases. Figure 6(a) shows the complementary occupation of  
 555 the cation sites without any particular modulation of the  $z$   
 556 coordinate. On the contrary, from the Fourier maps centered  
 557 at the oxygen positions [Fig. 6(b)], it is inferred that the site  
 558 splitting observed in the average structure is needed in order to  
 559 satisfy the coordination requirement of the  $\text{Mn}^{3+}$  Jahn-Teller  
 560 active cation. In fact, it is noted that when the Na and Mn swap  
 561 sites (cf. compositional modulation), the same happens in the

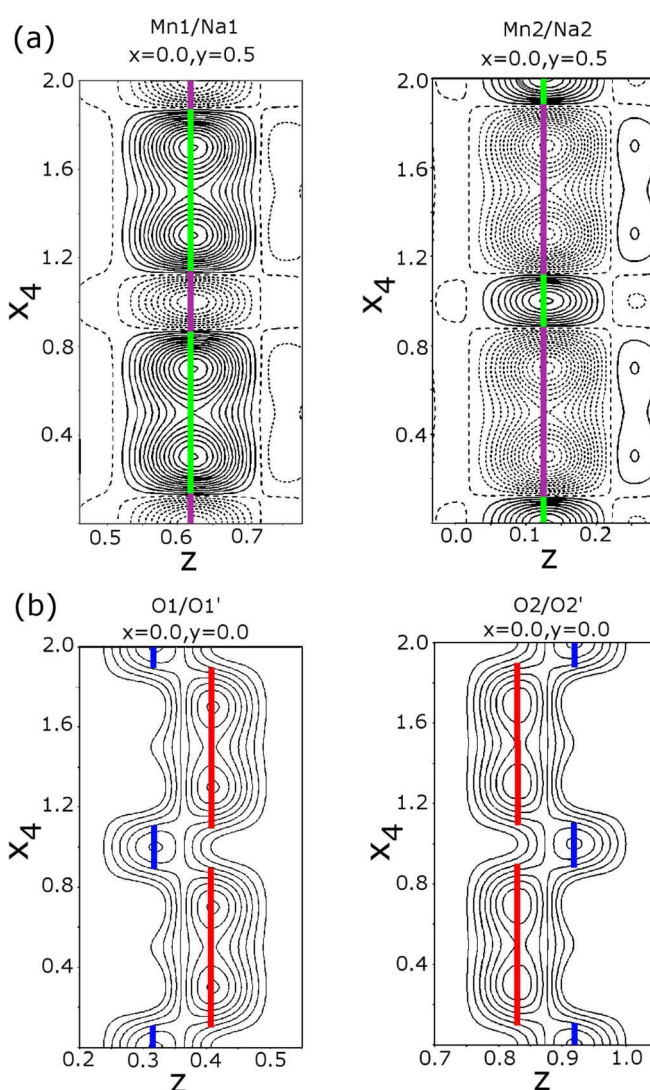


FIG. 6. Fourier maps of the observed structure factor ( $F_{\text{obs}}$ ) depicting the crystallographic cation sites (a) and oxygen positions (b). The solid colored lines represent the calculated position of the atoms showing no positional modulation along the  $x_4$  for the Mn/Na but its presence for the oxygen sites (violet Mn, green Na, red oxygen, and blue the primed oxygen position). The black continuous lines indicate the positive density isosurface and the dashed lines the negative isosurface (the neutron scattering length for the Mn atoms is negative). The isosurface contours correspond to two scattering density units ( $\text{\AA}^{-2}$ ) in all the plots.

oxygen split positions so that the bonding requirements are 562  
 restored as depicted in Fig. S3 [28]. Our approach demonstrates 563  
 that having taken advantage of the superspace formalism to 564  
 describe the compositional modulation of the Mn and Na sites 565  
 in a single-phase atomic configuration, the incommensurate 566  
 $\beta$ - $\text{NaMnO}_2$  structure can be depicted as a coherent intergrowth 567  
 of two types of  $\text{NaMnO}_2$  layers, reflecting the  $\alpha$ - and  $\beta$ - 568  
 polytype oxygen coordinations (Fig. 5). 569

#### D. Magnetic structure evolution 570

In view of the complex nuclear modulated structure observed 571  
 in the NPD profiles of  $\beta$ - $\text{NaMnO}_2$ , it is challenging to 572



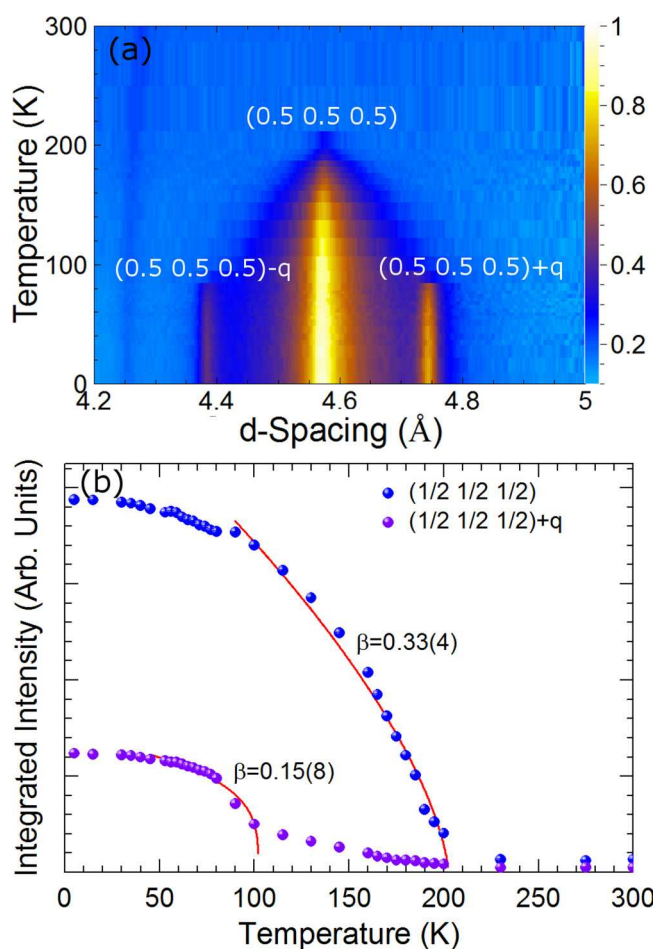


FIG. 7. (a) A long  $d$ -spacing section of the neutron powder diffraction patterns as a function of temperature, showing the complex nature of the magnetic contribution to the pattern. Color map: The neutron scattering intensity. (b) Integrated intensity versus temperature for the main magnetic reflections with propagation vector  $\mathbf{k} = (1/2, 1/2, 1/2)$ , and for the satellites with propagation vector  $\mathbf{k} + \mathbf{q}$ , where  $\mathbf{q} = (0.077(1), 0, 0)$ . The lines over the data points depict the fit to the critical region (see text).

573 evaluate the correlation between the crystal and magnetic structures as the sample temperature is lowered. The temperature  
 574 evolution of the diffraction pattern demonstrates the presence  
 575 of two magnetic transitions (Fig. 7).  
 576

577 First, below  $T_{N1} \sim 200$  K there is an intensity increase at  
 578 magnetic Bragg peak positions corresponding to a propagation  
 579 vector  $\mathbf{k} = (1/2, 1/2, 1/2)$  with respect to the  $Pmnm$  orthorhombic  
 580 average structure. These reflections grow quickly below the  
 581 magnetic transition temperature and their broad Lorentzian-like  
 582 profile is an indication that the magnetic domain is sensitive  
 583 to the strain and defects present in the nuclear structure  
 584 (refer to Fig. 6), complying with the broadening of  $^{23}\text{Na}$   
 585 NMR spectra [inset, Fig. 2(a)]. Moreover, below about 100 K  
 586 the diffraction patterns show the development of additional  
 587 reflections [Fig. 7(a)]. This new set of peaks can be indexed  
 588 assuming the combination of the magnetic propagation vector  
 589  $\mathbf{k}$  and the nuclear one  $\mathbf{q}$ , giving magnetic intensity at the  
 590 positions  $hkl \pm [\mathbf{k} \pm \mathbf{q}]$ . It is worth noting that the temperature  
 591 dependence of the integrated intensity [Fig. 7(b)] of these

two sets of reflections possesses different critical behavior,  
 thus suggesting that the two magnetic orders likely fall into  
 different universality classes. In particular, the fit of the  $1/2$   
 $1/2$   $1/2$  reflection with power law  $I = I_0[1 - (T/T_N)]^{2\beta}$  gives  
 a critical exponent of  $\beta = 0.33(4)$ , indicating interactions of  
 a 3D nature, instead, the  $\mathbf{k} \pm \mathbf{q}$  satellites possess an exponent  
 of  $\beta = 0.15(8)$ , which is more consistent with 2D interactions  
 [Fig. 7(b)]. Careful analysis of the diffraction pattern reveals  
 the presence of some additional low intensity reflections that  
 are not indexed with the previous propagation vectors. These  
 extra reflections are ascribed to a small content of MnO  
 impurity and the  $\alpha$ -polymorph.

Let us first discuss the important changes in the NPD  
 pattern that were observed below 200 K. In order to establish  
 the possible magnetic space group we performed magnetic  
 symmetry analysis with the help of the ISODISTORT software  
 [44]. The NPD patterns show that no clear magnetic intensity  
 is observed on the nuclear satellite reflections, therefore  
 pointing out that the magnetic structure is not strongly related  
 to the nuclear modulation at least in the  $100 < T < 200$   
 K temperature range. For this reason, magnetic symmetry  
 analysis was initiated on the basis of parent average  $Pmnm$   
 nuclear structure (Fig. S1, Table S1) [28] and the propagation  
 vector  $\mathbf{k} = (1/2, 1/2, 1/2)$ . The results of the symmetry analysis  
 are reported in Table S2 [28]. The best agreement between  
 observed and calculated patterns was obtained for the mR1  
 representation, with order parameter direction (OPD)  $P1(a, 0)$ ,  
 corresponding to the magnetic space group  $C_a2/c$ , with a  
 change in the unit cell with respect to the parent structure  
 described by the transformation matrix  $(0, -2, 0, 0, 2, -1, 1, 0)$ .  
 It is worth underlining that the space group  $C_a2$  also gives  
 a reasonably good result (Table S2), but with an increased

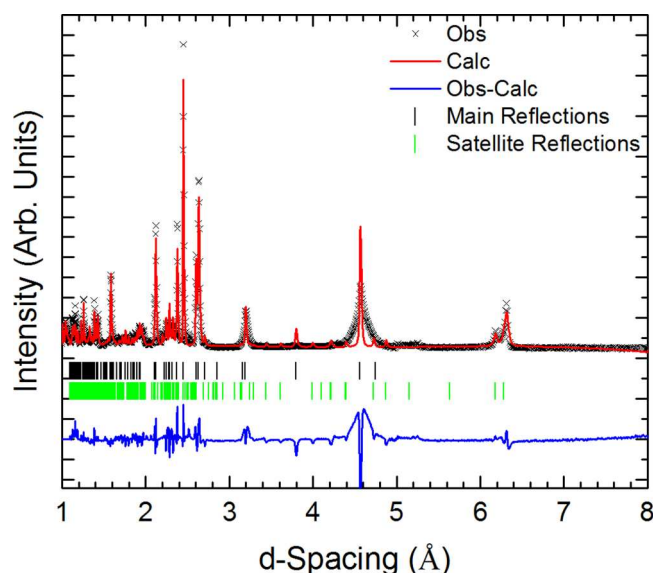


FIG. 8. Rietveld plot at 100 K of the  $\beta$ - $\text{NaMnO}_2$  structure in  $C_a2'/c'(\alpha 0 \gamma)00$  superspace group, with cell parameters  $a = 5.7108(2)$  Å,  $b = 12.6394(9)$  Å,  $c = 5.5397(4)$  Å,  $\beta = 120.96(7)^\circ$ , and  $\mathbf{q} = (0, 0, 0.078(1))$ . Observed (black crosses), calculated (red line), and difference (blue line) patterns are reported. The tick marks indicate the calculated position of the main (black ticks) and satellite reflections (green ticks).

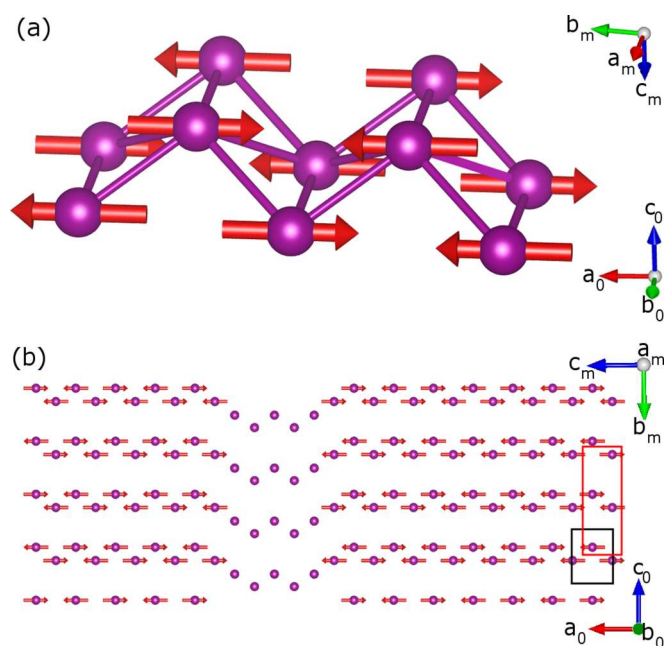


FIG. 9. Sketch of the magnetic structure below 200 K, (a) along the Mn zigzag chain typical of the  $\beta$ -polymorph ( $\mathbf{a}_0$  direction) and (b) in the same projection as for Fig. 6 (top panel). The black rectangle depicts the unit cell of the average  $Pmmn$  structure [ $a_0 = 4.7851(2)$  Å,  $b_0 = 2.85699(8)$  Å,  $c_0 = 6.3287(4)$  Å], while the red rectangle indicates the unit cell of the average low temperature monoclinic structure [ $a_m = 5.7112(2)$  Å,  $b_m = 12.6388(9)$  Å,  $c_m = 5.5365(4)$  Å,  $\beta = 120.97(7)^\circ$ ]; please note that the  $\mathbf{c}_m$  axis is inclined by  $\sim 60^\circ$  out of the plane.

number of refinable variables, thus suggesting the higher symmetry option  $C_a2/c$  as the best solution. Combining the mR1  $P1(a,0)$  IRs with the compositional modulated structure, the  $C_a2'/c'(a0\gamma)00$  magnetic superspace group is obtained. With the latter we then carried out Rietveld refinements, with the representative 100 K profile. The Rietveld plot is shown in Fig. 8, and the refined parameters are compiled in Table S3 [28]. The associated reliability factors are  $R_{F_{\text{obs}}} = 8.46\%$  for the nuclear reflections and  $R_{F_{\text{mag}}} = 12.50\%$  for the magnetic ones, while  $R_p = 13.88\%$ . Their values are rather on the high side, due to pronounced  $hkl$ -dependent broadening, likely arising from the presence of planar defects. The magnetic structure is drawn in Fig. 9, projected in the same plane as the nuclear one (Fig. 5, top panel). It entails antiferromagnetically coupled Mn chains running down the  $\mathbf{b}_0$  axis ( $\mathbf{a}_0$ ,  $\mathbf{b}_0$ , and  $\mathbf{c}_0$  setting is with respect to the orthorhombic  $Pmmn$  unit cell), stacked in a zigzag fashion when viewed in an  $a_0c_0$ -plane projection [Fig. 9(a)] that gives rise to antiferromagnetically coupled, corrugated  $\text{MnO}_2$  layers [Fig. 9(b)]. A similar collinear spin model has been utilized before for the description of the magnetic state in the isomorphous  $\beta$ - $\text{LiMnO}_2$ , where three-dimensional long-range order is established at  $T_N \sim 260$  K [55].

The derived spin configuration for  $\beta$ - $\text{NaMnO}_2$ , though, indicates a commensurate ordering only for the Mn2 site, as a similar ordering on the Mn1 site would have generated strong magnetic intensity at the nuclear satellite reflections, a case

that is not supported by the NPD data. In this compositionally modulated nuclear structure, between  $100 < T < 200$  K, only the  $\text{NaMnO}_2$  layer stacking sequences characteristic of the  $\beta$ -polytype carry a net magnetic moment. Such a magnetically inhomogeneous state is consistent with the wipeout of the central  $^{23}\text{Na}$ -NMR line [Fig. 2(b)] and the two-component nuclear spin-lattice relaxation in the same temperature range. The magnetic moment of Mn2 sites has been computed as  $\mu \cong 2.38(10)\mu_B$  at 100 K, but as the observed NPD profile shows fairly broad magnetic peaks, the attained staggered moment may be an underestimate (cf. the full moment for spin-2  $\text{Mn}^{3+}$  is expected to be  $4\mu_B$ ).

When temperature is lowered below  $T_{N2} \sim 100$  K, the incommensurate-like magnetic ordering appears to be described with a combination of the magnetic  $\mathbf{k}$  and nuclear  $\mathbf{q}$  propagation vectors suggesting that the second transition takes place because longer-range magnetic correlations are established in the alphas-like stacking sequence(s). Assuming that the same superspace group defines also the magnetic order at  $T < 100$  K and taking into account a Mn1-site spin configuration similar to that of the Mn2 site, magnetic scattering is calculated only for the  $\mathbf{k} + \mathbf{q}$  satellite positions. However, its relative intensity does not match the experimentally observed one, pointing out that additional spin modulation of the existing structure is required in order to adequately reproduce the observed magnetic NPD pattern. Rietveld refinements of the magnetic structure confirmed that the magnetic phase below  $T_{N2}$  can be described by a proper-screw component, with propagation vector  $\mathbf{k} + \mathbf{q}$  for both Mn1 and Mn2 sites, while refinements assuming a spin-density wave type of structure produced worse agreement factors and unphysical moment size for the Mn1 site. The corresponding Rietveld refined 5 K NPD profile is shown in Fig. 10, with the refined magnetic parameters compiled in Table S4 [27]. The associated reliability parameters are  $R_{F_{\text{obs}}} = 8.41\%$  for the nuclear reflections and  $R_{F_{\text{mag}}} = 9.4\%$  for the magnetic ones, while  $R_p = 16.6\%$  is relatively poor again due to the extreme peak broadening. The magnetic structure below  $T_{N2}$  is depicted in Figs. 11(a) and 11(b).

To a first approximation the spin configuration is similar to the commensurate one that develops below  $T_{N1}$ , but at the “boundary” of the  $\alpha$ - and  $\beta$ -like stacking sequences (Fig. 5), as the ordering at the Mn1 site ( $\alpha$ - $\text{NaMnO}_2$  layer stacking sequence) acts as a perturbation to the Mn2 site, the Mn spins start to rotate away from the commensurate structure type [Fig. 9(a)]. Within this modulated behavior, the  $\text{Mn}^{3+}$  magnetic moment takes the lowest values within the  $\text{NaMnO}_2$  layers characteristic of the  $\alpha$ -polytype (likely due to their higher degree of spin frustration), while it grows in magnitude as we move within the  $\beta$ -like stacking sequences, reaching a maximum  $\mu \cong 3.5(10)\mu_B$  at their midpoint (see Fig. S4) [28]. Such a nontrivial magnetic order is in line with very broad distribution of spin-lattice relaxation times found by NMR below  $T_{N2}$  (cf. low value of the stretching exponent), implying a broad distribution of local environments. This complexity might be an outcome of the system’s effort to relieve competing interactions among neighboring spins in the  $\beta$ - $\text{NaMnO}_2$  modulated nuclear structure, therefore requiring further insights on the role of geometric frustration.

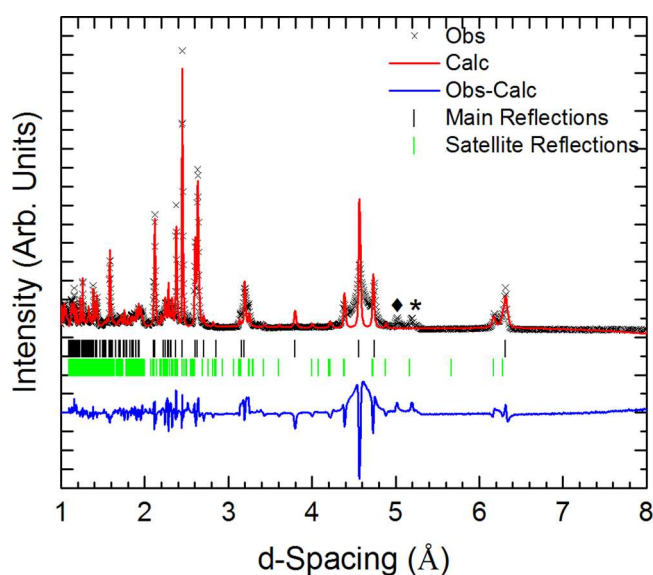


FIG. 10. Rietveld plot at 5 K for the  $\beta$ - $\text{NaMnO}_2$  structure in  $C_a2'/c'(a0\gamma)00$  superspace group, with cell parameters  $a = 5.7112(2)$  Å,  $b = 12.6388(9)$  Å,  $c = 5.5365(4)$  Å,  $\beta = 120.97(7)^\circ$ , and  $q = (0, 0, 0.081(1))$ . Observed (black crosses), calculated (red line), and difference (blue line) patterns are shown. The tick marks indicate the calculated position of the main (black ticks) and satellite reflections (green ticks). The asterisk marks the main nuclear and magnetic reflections from the  $\alpha$ - $\text{NaMnO}_2$  impurity phase, whereas the diamond indicates the main MnO magnetic reflection.

### E. Parametrization of magnetic excitations

711 Since the NPD and the NMR resolved two magnetic  
712 regimes, the magnetic fluctuations of  $\beta$ - $\text{NaMnO}_2$  were  
713 studied by inelastic neutron scattering (INS). An overview  
714

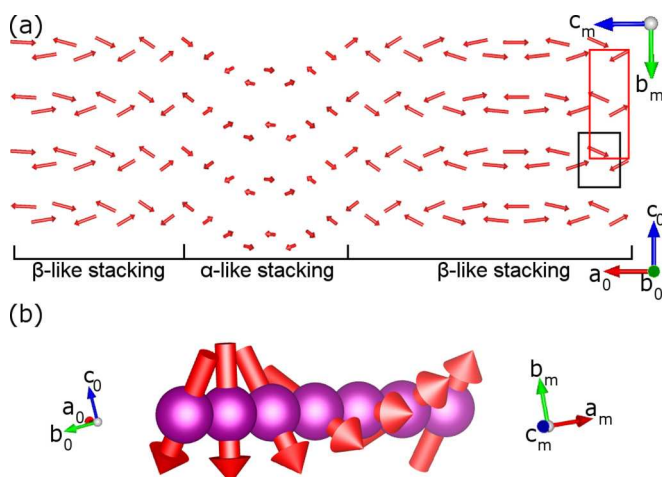


FIG. 11. (a) Schematic of the  $\beta$ - $\text{NaMnO}_2$  modulated magnetic structure at 5 K, projected at the same plane as the nuclear structure shown in Fig. 6 (top panel). (b) Sketch of the incommensurate part of the magnetic structure depicting a proper-screw order propagating along the  $(-110)$  direction with respect to the average  $Pmmn$  unit cell. In both panels the axes directions with subscript 0 indicate the average orthorhombic  $Pmmn$  cell (black rectangle), whereas the axes with subscript m indicate the direction of the low-temperature monoclinic structure (red rectangle).

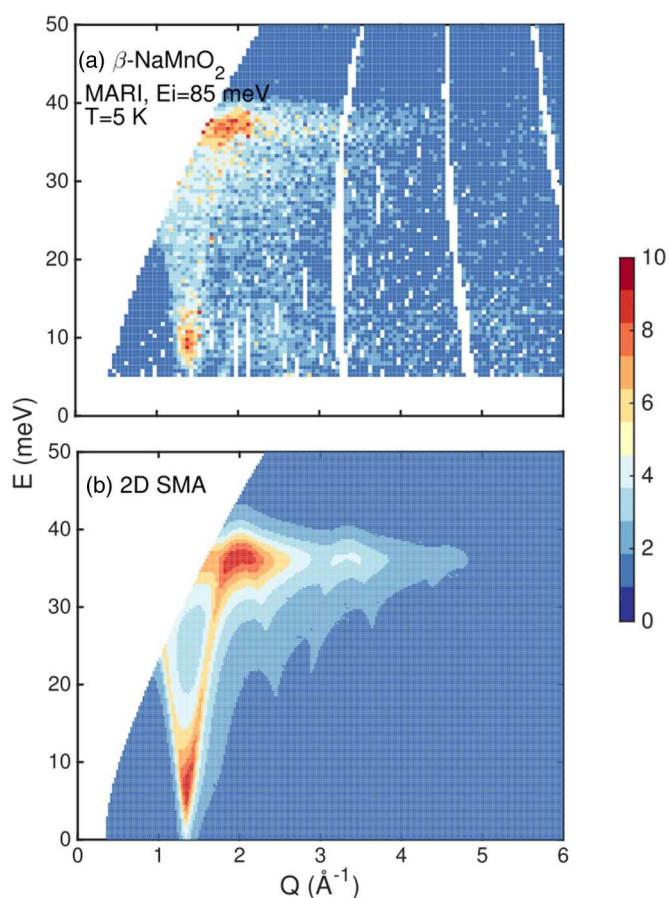


FIG. 12. (a) The powdered averaged magnetic scattering in  $\beta$ - $\text{NaMnO}_2$  and (b) the corresponding single mode approximation (SMA) heuristic model, with two-dimensional (2D) interactions. The background subtraction method to remove phonon scattering and instrument background are described in the text. Color map: The powder average scattering intensity  $\bar{I}(\vec{Q}, \hbar\omega)$  (see text for details).

of the measured INS response, well within the magnetically 715  
ordered state (5 K), is shown in Fig. 12(a) for experiments on 716  
the MARI spectrometer. A complementary insight on the low 717  
energy magnetic dynamics was offered with higher resolution 718  
through the DCS spectrometer (Fig. 13). At low temperatures 719  
(1.5 and 75 K) the DCS spectra show clearly the presence of a 720  
spin gap in the excitation spectrum, with little change in the gap 721  
energy,  $\Delta \sim 5$  meV. A pronounced change is observed at 100 K 722  
with a filling of the gap, yet with the presence of significant 723  
magnetic scattering even at  $T > T_{N1}$  (see Fig. S5) [28]. 724

As the measured neutron scattering cross section is propor- 725  
tional to the structure factor  $S(\vec{Q}, \hbar\omega)$ , for a powder 726  
material, the measured, momentum integrated neutron intensi- 727  
ty is proportional to the following average at a fixed  $|\vec{Q}|$ , 728  
 $\bar{I}(\vec{Q}, \hbar\omega) = \int \frac{d\Omega}{d\Omega} \frac{S(\vec{Q}, \hbar\omega)}{Q^2}$ . Obtaining microscopic exchange in- 729  
teractions that form the basis of the magnetic Hamiltonian 730  
from powder neutron data are rather difficult owing to the 731  
averaging over all reciprocal space directions  $|\vec{Q}|$ . However, 732  
applying sum rules allows information to be obtained about 733  
the interactions and correlations in a general way which is 734  
independent from the microscopic Hamiltonian. We outline 735  
this method in the following. 736

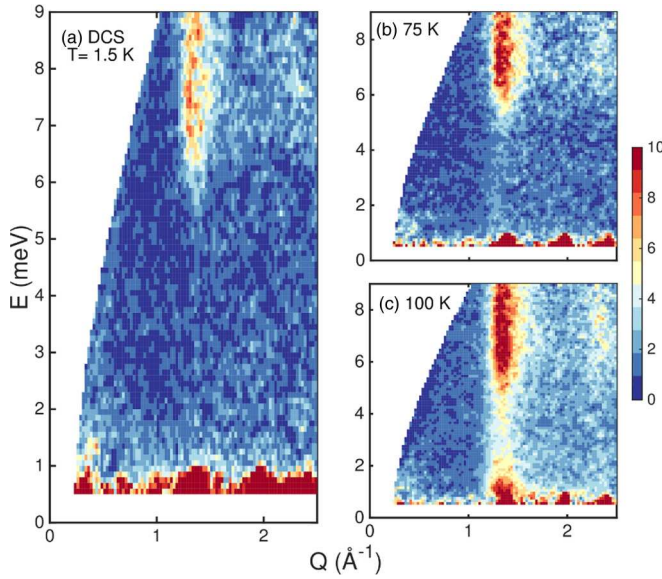


FIG. 13. The temperature dependence of the low-energy magnetic fluctuations in  $\beta$ - $\text{NaMnO}_2$ , measured on the high-resolution DCS spectrometer. All data has been corrected for a temperature independent background using the detailed balance relation. Color map: The powder average scattering intensity.

In the absence of a full theory for the magnetic exchange interactions in  $\beta$ - $\text{NaMnO}_2$ , and lack of single crystal data, we have parametrized the dispersion  $E(\vec{Q})$  with a phenomenological expression which satisfies the periodicity of the lattice and hence Bloch's theorem. One possible form of the dispersion, consistent with lattice periodicity, can be written as a Fourier series  $E^2(\vec{Q}) = \Delta + \sum_d B_d \sin^2(\vec{Q} \cdot \vec{d})$ , where  $\vec{d}$  is a bond vector connecting nearest-neighbor (NN) spins,  $B_d$  are coefficients in this series expansion, and  $\Delta$  is the magnitude of the spin gap. Because the magnetic excitations appear relatively sharp in energy (Figs. 12 and 13), we could utilize the single mode approximation (SMA) which states that the structure factor, which is proportional to the neutron cross section, is dominated by a single resonant mode.

The problem of deriving a parametrization of the neutron cross section  $S^{\alpha\alpha}(\vec{Q}, \hbar\omega) = S(\vec{Q})\delta[\hbar\omega - E(\vec{Q})]$  (delta function being numerically approximated by a Lorentzian with the energy resolution width), is reduced to finding an expression for  $S(\vec{Q})$ . To do this, we apply the Hohenberg-Brinkmann first moment sum rule [56], which applies to the case of isotropic exchange and is closely related to the ground state magnetic energy. Effectively the first moment sum relates  $S(\vec{Q})$  to the dispersion  $E(\vec{Q})$  through the following expression:

$$S(\vec{Q}) = \frac{\hbar\omega}{E(\vec{Q})} = -\frac{1}{3} \frac{1}{E(\vec{Q})} \sum_{\vec{d}} J_d \langle \vec{S}_0 \cdot \vec{S}_d \rangle [1 - \cos(\vec{Q} \cdot \vec{d})]. \quad (4)$$

In view of this, the single-mode approximation and parametrization of the dispersion  $E(\vec{Q})$  allows us to characterize which correlations are important and also determine the dimensionality of the excitations. In particular, the energy gap in a powder averaged constant- $Q$  scan is sensitive to the

dimensionality of the interactions. This fact was previously used to show that  $\alpha$ - $\text{NaMnO}_2$  is dominated by one-dimensional magnetic correlations [37].

Comparison of the powder averaged spectra for  $\beta$ - $\text{NaMnO}_2$  against its closely related  $\alpha$ - $\text{NaMnO}_2$  system (see Fig. S6) [28] points to several key differences. First, the spectral weight in  $\alpha$ - $\text{NaMnO}_2$  is concentrated at low energies near the energy gap edge, while it is much more evenly distributed in energy in the case of the  $\beta$ - $\text{NaMnO}_2$  variant. The scattering is also much more strongly peaked [56] in momentum for  $\beta$ - $\text{NaMnO}_2$ , which is indicative of the higher (cf. than the quasi-1D of the  $\alpha$  phase) dimensionality of the associated spin correlations. In addition, considerable spectral weight is located at the top of the excitation band and the scattering is much more well defined in momentum than in the  $\alpha$ -polytype. Such qualitative observations suggest that  $\beta$ - $\text{NaMnO}_2$  may be more two dimensional than the  $\alpha$  phase. We have therefore simulated the powder averaged spectra by considering the case of the two-dimensional spin exchange, with dominant correlations along the  $\mathbf{b}_0$ -crystal axis. We have taken the dispersion relation to have the following phenomenological expression:

$$E^2(\vec{Q}) = B_0 + B_1 \sin^2(\pi K) + B_2 \sin^2(\pi H) + \dots + B_3 \{\sin^2[\pi(K + H)] + \sin^2[\pi(K - H)]\}, \quad (5)$$

which is consistent with the periodicity of the lattice ( $Pmnn$  symmetry) and gives a minimum at half-integer positions, relating the observed magnetic Bragg peaks. We have chosen  $B_0 = 25 \text{ meV}^2$  to account for the spin-gap ( $\Delta$ ),  $B_1 = B_2 = 625 \text{ meV}^2$  and  $B_3 = 400 \text{ meV}^2$ .

To extract an estimate for the exchange constants, we have put the inelastic magnetic response on an absolute scale using the internal incoherent elastic line as a reference. The absolute calibration combined with the first moment sum rule afforded an estimate of  $J_d \langle S_0 \cdot S_d \rangle$ . Combined with the collinear magnetic structure, we have estimated a strong exchange along the  $\mathbf{b}_0$ ,  $J_1 = 5.0 \pm 1.0 \text{ meV}$ , and a weaker one along  $\mathbf{a}_0$ ,  $J_3 = 1.5 \pm 1.0 \text{ meV}$  (Fig. S1) [28].

The total integrated spectral weight (elastic and inelastic) is constrained by the zeroth moment sum rule which can be summarized as follows:

$$\frac{\int d^3q S(\vec{Q}, \hbar\omega)}{\int d^3q} = S(S + 1). \quad (6)$$

Integrating the INS data by using the elastic incoherent scattering of the vanadium as an internal standard gives the inelastic contribution to the above integral being 1.8(3). Including the ordered moment in the elastic channel and noting that there are two  $\text{Mn}^{3+}$  ions per unit cell gives a total integral of 4.7(4) for this sum. Given the expected value for  $S = 2$  is 12, this indicates that more than half of total moment resides elsewhere in momentum and energy. One possibility is for a large fraction residing in diffuse scattering, which maybe resulting in a low-energy contribution that is beyond the resolution of the spectrometer, while it is in agreement with the broad shape of the magnetic reflections in the diffraction data and with the high density of structural defects present in the material.

### F. Incommensurate structure and frustration

We have seen that the magnetic long-range order of  $\beta$ - $\text{NaMnO}_2$  is strongly correlated with its structural complexity, which is established through the relief of frustration. Importantly, competing interactions between spins and their complex magnetic orders are known to motivate spectacular cross-coupling effects that lead to improper ferroelectricity in frustrated magnets [57]. Establishing cross control of the magnetic and ferroelectric polarizations challenges scientific endeavors as striking new multiferroic device concepts may be realized [58]. A key question then is whether the compositionally modulated nuclear structure and magnetic order in  $\beta$ - $\text{NaMnO}_2$  may also stimulate competing degrees of freedom that can become cross correlated through the symmetries [59] of the associated magnetic and nuclear orderings. Preliminary evidence for such a type of behavior in  $\beta$ - $\text{NaMnO}_2$  was first reported by Bakaimi *et al.* who demonstrated that the temperature-dependent dielectric permittivity  $\epsilon'(T)$  displays two small anomalies, near the  $T_{N1}$  and  $T_{N2}$  transitions discussed here [60]. Since the explanation of possible magnetoelectric coupling needs the understanding of the crystal and magnetic symmetries, these early findings remained unexplored. Now that these structures are known, through the current work, it is worth revisiting the coupling of the aforementioned properties.

Let us now glance through the dielectric response of  $\beta$ - $\text{NaMnO}_2$  and compare it to that of  $\alpha$ - $\text{NaMnO}_2$ . Bearing in mind that the magnitude of the dielectric permittivity anomalies in  $\beta$ - $\text{NaMnO}_2$  becomes larger with the application of an intense electric field [60], here instead we utilized a progressively stronger external magnetic field, hoping for enhanced changes in the  $\epsilon'(T)$ . Our dielectric permittivity experiments, however, identified only small anomalies in  $\epsilon'(T, H)$  curves that coincide with the onset of antiferromagnetic orders taking place in the bulk  $\alpha$  ( $T_N = 45$  K) and  $\beta$  ( $T_{N2} = 95$  K) phases. In  $\beta$ - $\text{NaMnO}_2$ , no other low-temperature  $\epsilon'(T, H)$  signature is observed that could indicate contributions from  $\alpha$ - and  $\beta$ -type structural domains, as local probes have resolved before [41]. Moreover, the magnetoelectric coupling must be weak in both  $\text{NaMnO}_2$  materials, as very little changes are brought about despite the strength of the externally applied magnetic field (Fig. 14). Having taken into account the symmetry-imposed constraints for the free-energy [61] in the  $\alpha$ - and  $\beta$ -magnetic phases, it is conferred that the spatial inversion symmetry is not violated, excluding the possibility of improper ferroelectricity in the magnetically ordered states (see Sec. S7, Supplemental Material). In this respect, it is postulated that the observed small anomalies in the dielectric constant are likely related to the nonlinear, higher order terms (e.g., biquadratic term  $\sim E^2 H^2$ ) that are operative in chemically diverse systems, ranging from planar magnets [62,63] and three-dimensional magnetoelectric perovskites ( $\text{AMnO}_3$ ,  $A = \text{Y, Bi}$ ) [64,65] to quantum paraelectrics ( $\text{EuMeO}_3$ ) [66,67].

### IV. SUMMARY AND CONCLUSIONS

The present work entails a thorough study of the crystallographic and dynamical properties of  $\beta$ - $\text{NaMnO}_2$ . The proposed single-phase nuclear structure model takes advantage of the superspace formalism to describe the incommensurate compo-

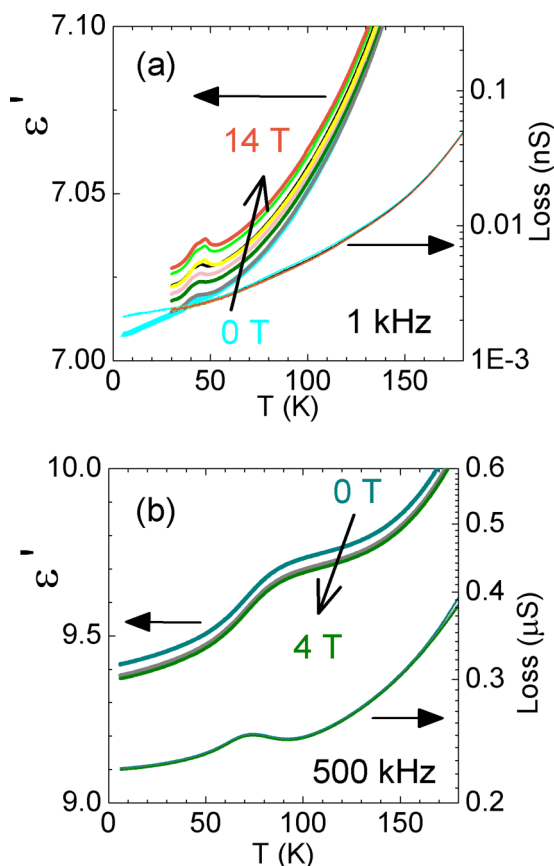


FIG. 14. Temperature dependent dielectric permittivity  $\epsilon'(T)$  as a function of the applied magnetic field for  $\alpha$ - $\text{NaMnO}_2$  (a) and  $\beta$ - $\text{NaMnO}_2$  (b).

sitional modulation [propagation vector,  $\mathbf{q} = (0.077(1), 0, 0)$ ] of the Mn and Na sites that can be depicted as an intergrowth  $\alpha$ - and  $\beta$ -like oxygen coordinations. This peculiar topology strongly influences the physical and chemical properties of the material and underlines the role of the nearly degenerate in energy  $\alpha$  and  $\beta$  layer stacking sequences. The remarkable flexibility of  $\beta$ - $\text{NaMnO}_2$  to adapt its lattice topology is likely at the basis of the particular high charge capacity of the system as a Na-ion cathode material [35], but also may corroborate to the stability of the various nonstoichiometric phases [41] accessible through its electrochemical Na-intercalation/removal [68].

Moreover, the magnetic structure of  $\beta$ - $\text{NaMnO}_2$  was solved on the basis of time-of-flight neutron powder diffraction data and found to be strongly mediated by the material's inherent lattice topology. First, below  $T_{N1}$  (200 K), a collinear commensurate antiferromagnetic state, involving only the  $\beta$ -like stacking sequences, develops with a propagation vector  $\mathbf{k} = (1/2, 1/2, 1/2)$ . Then, a second magnetic transition is observed at  $T_{N2}$  (95 K), marked by new satellite reflections ascribed to the interaction of  $\mathbf{k}$  with the compositional modulation vector  $\mathbf{q}$ . The new magnetic ordering is due to the relief of the magnetic frustration in the  $\alpha$ -like sheets that in turn influences the ordering in the  $\beta$ -like stacking sequences, and instigates a cooperative proper-screw magnetic state. Here the lattice topology of the Jahn-Teller active  $\text{Mn}^{3+}$  cation drives

899 the original 3D spin correlations ( $T < T_{N1}$ ) to become 2D in  
 900 character. Inelastic neutron scattering and  $^{23}\text{Na}$  NMR provide  
 901 evidence that a spin gap ( $\Delta = 5$  meV) opens in the excitation  
 902 spectra, in line with the 2D nature of the magnetic interactions  
 903 at  $T < T_{N2}$ .

904 Overall, structure and dynamics point that the incommen-  
 905 surate  $\beta$ - $\text{NaMnO}_2$  structure can relay a magnetocapacitance  
 906 effect in the low-temperature magnetic state. Such a structural  
 907 complexity inquires whether controlled engineering of coher-  
 908 ent defects may impart the material with novel technological  
 909 capabilities. In view of this, it is worth considering that in the  
 910 compositionally modulated  $\beta$ - $\text{NaMnO}_2$ , domain-wall (DW)-  
 911 like phenomena [69] associated with the abundance of the  $\alpha$   
 912 and  $\beta$  interfaces (Figs. 6 and 12), rather than extended domains  
 913 themselves, may be the active element in promoting some  
 914 degree of topologically correlated (related to DW), cooperative  
 915 magnetic and electric dipole arrangements. The way electronic  
 916 structure changes at such interfacial regions could be relevant  
 917 in order to manipulate the magnetoelectric response [70] even

in this class of nonperovskite compounds and warrants further  
 918 exploration. 919

#### ACKNOWLEDGMENTS 920

We thank the Science and Technology Council (STFC) for  
 921 the provision of neutron beam time at ISIS Facility. Access to  
 922 DCS was provided by the Center for High Resolution Neutron  
 923 Scattering, a partnership between the National Institute of  
 924 Standards and Technology and the National Science Founda-  
 925 tion under Agreement No. DMR-1508249. This work was  
 926 partly funded by the Carnegie Trust for the Universities of  
 927 Scotland, the Royal Society, and the EPSRC. Partial funding  
 928 was also secured through the framework of the Heracleitus  
 929 II project (Grant No. 349309.WP1.56) co-financed by the  
 930 Ministry of Education and Religious Affairs, Greece and the  
 931 European Social Fund, European Union (Operational Program  
 932 “Education and Lifelong Learning” of the National Strategic  
 933 Reference Framework, NSRF, 2007–2013). 934

FQ

- 
- [1] W. Eerenstein, N. D. Mathur, and J. F. Scott, *Nature (London)* **442**, 759 (2006).
- [2] T. Kimura, T. Goto, H. Shintani, K. Ishizaka, T. Arima, and Y. Tokura, *Nature (London)* **426**, 55 (2003).
- [3] T. Goto, T. Kimura, G. Lawes, A. P. Ramirez, and Y. Tokura, *Phys. Rev. Lett.* **92**, 257201 (2004).
- [4] M. Pregelj *et al.*, *Phys. Rev. Lett.* **103**, 147202 (2009).
- [5] J. P. Parant, R. Olazcuag, M. Devalett, C. Fouassie, and P. J. Hagenmul, *Solid State Chem.* **3**, 1 (1971).
- [6] M. A. Marquardt, N. A. Ashmore, and D. P. Cann, *Thin Solid Films* **496**, 146 (2006).
- [7] H. Kawazoe, M. Yasukawa, H. Hyodo, M. Kurita, H. Yanagi, and H. Hosono, *Nature (London)* **389**, 939 (1997).
- [8] K. Takada, H. Sakurai, E. Takayama-Muromachi, F. Izumi, R. A. Dilanian, and T. Sasaki, *Nature (London)* **422**, 53 (2003).
- [9] C. Delmas, J. J. Braconnier, C. Fouassier, and P. Hagenmuller, *Solid State Ionics* **3–4**, 165 (1981).
- [10] N. Terada, Y. Ikedo, H. Sato, D. D. Khalyavin, P. Manuel, A. Miyake, A. Matsuo, M. Tokunaga, and K. Kindo, *Phys. Rev. B* **96**, 035128 (2017).
- [11] N. Terada, D. D. Khalyavin, P. Manuel, Y. Tsujimoto, K. Knight, P. G. Radaelli, H. S. Suzuki, and H. Kitazawa, *Phys. Rev. Lett.* **109**, 097203 (2012).
- [12] R. J. Clement, P. G. Bruce, and C. P. Grey, *J. Electrochem. Soc.* **162**, A2589 (2015).
- [13] C. Fouassier, G. Matejka, J. M. Reau, and P. Hagenmuller, *J. Solid State Chem.* **6**, 532 (1973).
- [14] J. M. Paulsen, R. A. Donabarger, and J. R. Dahn, *Chem. Mater.* **12**, 2257 (2000).
- [15] C. Delmas, C. Fouassier, and P. Hagenmuller, *Physica B & C* **99**, 81 (1980).
- [16] A. Janner and T. Janssen, *Phys. Rev. B* **15**, 643 (1977).
- [17] N. Choudhury, L. Walizer, S. Lisenkov, and L. Bellaiche, *Nature (London)* **470**, 513 (2011).
- [18] L. Righi, F. Albertini, L. Pareti, A. Paoluzi, and G. Calestani, *Acta Mater.* **55**, 5237 (2007).
- [19] L. Righi, F. Albertini, E. Villa, A. Paoluzi, G. Calestani, V. Chernenko, S. Besseghini, C. Ritter, and F. Passaretti, *Acta Mater.* **56**, 4529 (2008).
- [20] T. Kimura, *Annu. Rev. Mater. Res.* **37**, 387 (2007).
- [21] J. M. Perez-Mato, G. Madariaga, and M. J. Tello, *Phys. Rev. B* **30**, 1534 (1984).
- [22] J. M. Perez-Mato, J. L. Ribeiro, V. Petricek, and M. I. Aroyo, *J. Phys-Condens Matter* **24**, 163201 (2012).
- [23] W. Slawinski, R. Przenioslo, I. Sosnowska, M. Bieringer, I. Margiolaki, and E. Suard, *Acta Crystallogr. Sect. B* **65**, 535 (2009).
- [24] F. Orlandi, L. Righi, C. Ritter, C. Pernechele, M. Solzi, R. Cabassi, F. Bolzoni, and G. Calestani, *J. Mater. Chem. C* **2**, 9215 (2014).
- [25] I. Urcelay-Olabarria, J. M. Perez-Mato, J. L. Ribeiro, J. L. Garcia-Munoz, E. Ressouche, V. Skumryev, and A. A. Mukhin, *Phys. Rev. B* **87**, 014419 (2013).
- [26] Y. Takeda, J. Akagi, A. Edagawa, M. Inagaki, and S. Naka, *Mater. Res. Bull.* **15**, 1167 (1980).
- [27] M. Jansen and R. Hoppe, *Z. Anorg. Allg. Chem.* **399**, 163 (1973).
- [28] See Supplemental Material at <http://link.aps.org/supplemental/10.1103/PhysRevMaterials.xx.xxxxxx> for additional figures and tables with crystallographic information.
- [29] R. Hoppe, G. Brachtel, and M. Jansen, *Z. Anorg. Allg. Chem.* **417**, 1 (1975).
- [30] I. J. Davidson, R. S. Mcmillan, J. J. Murray, and J. E. Greedan, *J. Power Sources* **54**, 232 (1995).
- [31] A. R. Armstrong and P. G. Bruce, *Nature (London)* **381**, 499 (1996).
- [32] O. I. Velikokhatnyi, C. C. Chang, and P. N. Kumta, *J. Electrochem. Soc.* **150**, A1262 (2003).
- [33] A. M. Abakumov, A. A. Tsirlin, I. Bakaimi, G. Van Tendeloo, and A. Lappas, *Chem. Mater.* **26**, 3306 (2014).
- [34] R. Dally *et al.*, *J. Cryst. Growth* **459**, 203 (2017).

- [35] J. Billaud, R. J. Clement, A. R. Armstrong, J. Canales-Vazquez, P. Rozier, C. P. Grey, and P. G. Bruce, *J. Am. Chem. Soc.* **136**, 17243 (2014).
- [36] M. Giot, L. C. Chapon, J. Androulakis, M. A. Green, P. G. Radaelli, and A. Lappas, *Phys. Rev. Lett.* **99**, 247211 (2007).
- [37] C. Stock, L. C. Chapon, O. Adamopoulos, A. Lappas, M. Giot, J. W. Taylor, M. A. Green, C. M. Brown, and P. G. Radaelli, *Phys. Rev. Lett.* **103**, 077202 (2009).
- [38] A. Zorko, S. El Shawish, D. Arcon, Z. Jaglicic, A. Lappas, H. van Tol, and L. C. Brunel, *Phys. Rev. B* **77**, 024412 (2008).
- [39] A. Zorko, O. Adamopoulos, M. Komelj, D. Arcon, and A. Lappas, *Nat. Commun.* **5**, 3222 (2014).
- [40] A. Zorko, J. Kokalj, M. Komelj, O. Adamopoulos, H. Luetkens, D. Arcon, and A. Lappas, *Sci. Rep.-Uk* **5**, (2015).
- [41] R. J. Clement, D. S. Middlemiss, I. D. Seymour, A. J. Ilott, and C. P. Grey, *Chem. Mater.* **28**, 8228 (2016).
- [42] L. C. Chapon, P. Manuel, P. G. Radaelli, C. Benson, L. Perrott, S. Ansell, N. J. Rhodes, D. Raspino, D. Duxbury, E. Spill, and J. Norris, *Neutron News* **22**, 22 (2011).
- [43] V. Petricek, M. Dusek, and L. Palatinus, *Z. Krist.-Cryst. Mater.* **229**, 345 (2014).
- [44] B. J. Campbell, H. T. Stokes, D. E. Tanner, and D. M. Hatch, *J. Appl. Crystallogr.* **39**, 607 (2006).
- [45] C. Stock, E. E. Rodriguez, and M. A. Green, *Phys. Rev. B* **85**, 094507 (2012).
- [46] N. S. Kini, E. E. Kaul, and C. Geibel, *J. Phys.-Condens. Matter* **18**, 1303 (2006).
- [47] K. M. Ranjith, R. Nath, M. Majumder, D. Kasinathan, M. Skoulatos, L. Keller, Y. Skourski, M. Baenitz, and A. A. Tsirlin, *Phys. Rev. B* **94**, 014415 (2016).
- [48] A. Suter, M. Mali, J. Roos, and D. Brinkmann, *J. Phys.-Condens. Matter* **10**, 5977 (1998).
- [49] J. M. Perez-Mato, M. Zakhour-Nakhl, F. Weill, and J. Darriet, *J. Mater. Chem.* **9**, 2795 (1999).
- [50] V. Petricek, A. Vanderlee, and M. Evain, *Acta Crystallogr. Sect. A* **51**, 529 (1995).
- [51] P. M. D. Wolff, *Acta Crystallogr. Sect. A* **A33**, 493 (1977).
- [52] P. M. De Wolff, *Acta Crystallogr. Sect. A* **A30**, 777 (1974).
- [53]  $\sigma$  is the allowed direction of the order parameter in the distortion vector space defined by the irreducible representations within ISODISTORT suite.
- [54] S. v. Smaalen, *Incommensurate Crystallography* (Oxford University Press, New York, 2007).
- [55] J. E. Greedan, N. P. Raju, and I. J. Davidson, *J. Solid State Chem.* **128**, 209 (1997).
- [56] P. C. Hohenberg and W. F. Brinkman, *Phys. Rev. B* **10**, 128 (1974).
- [57] S. W. Cheong and M. Mostovoy, *Nat. Mater.* **6**, 13 (2007).
- [58] Y. H. Chu *et al.*, *Nat. Mater.* **7**, 478 (2008).
- [59] M. Fiebig, *J. Phys. D Appl. Phys.* **38**, R123 (2005).
- [60] I. Bakaimi, A. Abakumov, M. A. Green, and A. Lappas, in *SPIE OPTO* (SPIE, Bellingham, WA, 2014), p. 7.
- [61] G. A. Smolenskii and I. E. Chupis, *Usp Fiz Nauk* **137**, 415 (1982).
- [62] D. L. Fox, D. R. Tilley, J. F. Scott, and H. J. Guggenheim, *Phys. Rev. B* **21**, 2926 (1980).
- [63] G. A. Samara and J. F. Scott, *Solid State Commun.* **21**, 167 (1977).
- [64] T. Katsufuji, S. Mori, M. Masaki, Y. Moritomo, N. Yamamoto, and H. Takagi, *Phys. Rev. B* **64**, 104419 (2001).
- [65] T. Kimura, S. Kawamoto, I. Yamada, M. Azuma, M. Takano, and Y. Tokura, *Phys. Rev. B* **67**, 180401 (2003).
- [66] V. V. Shvartsman, P. Borisov, W. Kleemann, S. Kamba, and T. Katsufuji, *Phys. Rev. B* **81**, 064426 (2010).
- [67] R. Saha, A. Sundaresan, M. K. Sanyal, C. N. R. Rao, F. Orlandi, P. Manuel, and S. Langridge, *Phys. Rev. B* **93**, 014409 (2016).
- [68] A. Mendiboure, C. Delmas, and P. Hagenmuller, *J. Solid State Chem.* **57**, 323 (1985).
- [69] M. Daraktchiev, G. Catalan, and J. F. Scott, *Phys. Rev. B* **81**, 224118 (2010).
- [70] J. Seidel *et al.*, *Nat. Mater.* **8**, 229 (2009).